Acoustic emissions of nearly steady and uniform granular flows: A proxy for flow dynamics and velocity fluctuations

Vincent Bachelet, Anne Mangeney, Renaud Toussaint, Julien de Rosny, Mattew I. Arran, Maxime Farin, Clément Hibert

JGR Earth Surface

RESEARCH ARTICLE
10.1029/2022JF006990

Acoustic Emissions of Nearly Steady and Uniform Granular Flows: A Proxy for Flow Dynamics and Velocity Fluctuations

V. Bachelet[1], A. Mangeney[1], R. Toussaint[2,3], J. de Rosny[4], M. I. Arran[1,5], M. Farin[4], and C. Hibert[2]

[1]Université Paris Cité, Institut de Physique du Globe de Paris, CNRS, Paris, France, [2]University of Strasbourg, CNRS, Institut Terre et Environnement de Strasbourg, UMR 7063, Strasbourg, France, [3]PoreLab, Njord Centre, Department of Physics, University of Oslo, Oslo, Norway, [4]Institut Langevin, ESPCI Paris, Université PSL, CNRS, Paris, France, [5]LSRI, Campion Hall, University of Oxford, Oxford, UK

Key Points:

- We analyze the high-frequency emissions and particle agitation of quasi-steady granular flows on constant slopes
- Scaling laws between granular temperature, average velocity, shear rate and inertial number are derived
- A simple physical model for the acoustic emissions and acoustic efficiency of steady flows is developed and tested

Supporting Information:

Supporting Information may be found in the online version of this article.

Correspondence to:

R. Toussaint,
renaud.toussaint@unistra.fr

Citation:

Bachelet, V., Mangeney, A., Toussaint, R., de Rosny, J., Arran, M. I., Farin, M., & Hibert, C. (2023). Acoustic emissions of nearly steady and uniform granular flows: A proxy for flow dynamics and velocity fluctuations. *Journal of Geophysical Research: Earth Surface*, *128*, e2022JF006990. https://doi.org/10.1029/2022JF006990

Received 19 NOV 2022
Accepted 21 FEB 2023

Abstract The seismic waves emitted during granular flows are generated by different sources: high frequencies by interparticle collisions and low frequencies by global motion and large scale deformation. To unravel these different mechanisms, an experimental study has been performed on the seismic waves emitted by dry, dense, quasi-steady granular flows. The emitted seismic waves were recorded using shock accelerometers and the flow dynamics were captured with a fast camera. The mechanical characteristics of the particle collisions were analyzed, along with the intervals between collisions and the correlations in particles' motion. The high-frequency seismic waves (1–50 kHz) were found to originate from particle collisions and waves trapped in the flowing layer. The low-frequency waves (20–60 Hz) were generated by particles' oscillations along their trajectories, that is, from cycles of dilation/compression during coherent shear. The profiles of granular temperature (i.e., the mean squared value of particle velocity fluctuations) and average velocity were measured and related to each other, then used in a simple steady granular flow model, in which the seismic signal consists of the variously attenuated contributions of shear-induced Hertzian collisions throughout the flow, to predict the rate at which seismic energy was emitted. Agreement with the measured seismic power was reasonable, and scaling laws relating the seismic power, the shear strain rate and the inertial number were derived. In particular, the emitted seismic power was observed to be approximately proportional to the root mean square velocity fluctuation to the power 3.1 ± 0.9, with the latter related to the mean flow velocity.

Plain Language Summary The generation of seismic waves during granular avalanches is studied experimentally and compared to simple models. The experiments allow granular layers to reach a steady state, waves are recorded through the basement with accelerometers and grain motion is followed with a fast camera. The origin of the different frequencies of signals is discussed. The role of the particles' collisions and the attenuation of the waves in the layer is investigated.

1. Introduction

Gravitational flows such as landslides, debris avalanches, and rockfalls represent one of the major natural hazards threatening life and property in mountainous, volcanic, seismic, and coastal areas, with large events possibly displacing several hundred thousand people. They play a key role in erosion processes on the Earth's surface. Gravitational instabilities are also closely related to volcanic, seismic, and climatic activity and thus represent potential precursors or proxies for changes in these activities with time, as shown, for example, for the Piton de la Fournaise volcano, Réunion (Durand et al., 2018; Hibert, Mangeney, et al., 2017; Hibert et al., 2014) or for the Soufrière Hills volcano, Montserrat (Calder et al., 2005; Levy et al., 2015).

Research involving the dynamic analysis of gravitational mass flows is advancing rapidly. One of its ultimate goals is to produce tools for detecting natural instabilities and for predicting the velocity, dynamic pressure, and runout extent of rapid landslides. However, the theoretical description and physical understanding of these processes in a natural environment are still open and extremely challenging problems (see Delannay et al. (2017) for a review). In particular, the origin of the high mobility of large landslides is still unexplained, with different hypotheses proposed in the literature (acoustic fluidization, flash heating, etc.) (Lucas et al., 2014). The lack of field measurements relevant to the dynamics of natural landslides prevents us from fully understanding the processes involved and from predicting landslide dynamics and deposition. Indeed, these events are generally

unpredictable but have a strongly destructive power. Furthermore, data on the deposits are not always available due to subsequent flows, erosion processes, or site inaccessibility.

In this context, analysis of the seismic signal generated by natural instabilities provides a unique way to detect and characterize these events and to discriminate between the physical processes involved. When flowing down the slope, landslides generate seismic waves in a wide frequency range that are recorded by local, regional, or global seismic networks, depending on the event size (Allstadt et al., 2018; Okal, 1990). As a result, the recorded seismic signal, with frequencies ranging from about 0.006 to 30 Hz, carries key information on landslide dynamics to distances far from the source. However, the characterization of landslides from their seismic signals suffers from uncertainty about the respective effects on such signals of mean flow dynamics, grain-scale processes, topographic variation, and wave propagation. It is commonly speculated that grain impacts on the substrate generate high frequencies (>1 Hz in geophysical contexts), while the mean flow acceleration/deceleration is responsible for lower frequencies.

Regarding the terminology in this work, we monitor the elastic (mechanical) waves transmitted to the solid plate under the flow. They arise due to the motion of the flowing grains and are transmitted to the plate mostly by the grains in contact with the plate. Some conversion of waves transmitted in the air to waves transmitted in the grains or plate is also possible, but any such converted waves are presumably small in amplitude compared to the waves transmitted entirely via the solid grains. Concerning the terminology, researchers in the acoustic community use the term "acoustic wave" for all mechanical waves, whether in gas, solid, or liquid. Researchers in geophysics and seismology use the term "acoustic wave" for waves propagating in a gas or liquid, and "seismic wave" for waves in a solid. Most articles studying waves in solids generated during granular flow term them "acoustic," without distinction of the propagation medium, and most articles studying waves generated at field scale by avalanches or debris flow term them "seismic." Hence, we adopt this terminology and will refer to the monitored waves as acoustic waves or elastic waves at the laboratory scale and seismic waves at the field scale.

Much work has been devoted to extracting information on geophysical flow dynamics from low-frequency signals (periods 10 s $< \tau <$ 120 s), with the net force that a landslide applies to the ground recovered using signal deconvolution, for example, Allstadt (2013), Ekström and Stark (2013), Hibert, Ekström, and Stark (2017), Kanamori and Given (1982), La Rocca et al. (2004), Lin et al. (2010), Moretti et al. (2012), Yamada et al. (2013), and Zhao et al. (2015). The time history of this force is directly related to the acceleration and deceleration of the flow along the topography. Comparing this force with the force simulated with landslide models makes it possible to recover a landslide's characteristics and dynamics, such as its volume and timing, the friction coefficients involved, the role of erosion processes, and the underlying ground's composition (rock or ice) and topography (Favreau et al., 2010; Moretti et al., 2020, 2015, 2012; Schneider et al., 2010; Yamada et al., 2018, 2016).

The high-frequency signal is much more difficult to interpret, due in part to the strong effect of topography and Earth heterogeneity along seismic waves' path from source to receiver (Kuehnert et al., 2020, 2021). For this reason, mainly empirical relationships have been proposed between high-frequency signals and landslide characteristics (Allstadt et al., 2020; Dammeier et al., 2011; Deparis et al., 2008; Norris, 1994). However, high-frequency signals are recorded more commonly than low-frequency signals, because of the lower price of short period seismometers and because small landslides (with volumes $<10^7$ m^3 (Allstadt et al., 2018)) only generate frequencies larger than about 1 Hz. Recent studies show correlations between the high-frequency signal (energy, envelope, etc.) and the mean properties of the flow (potential energy lost, force, velocity, momentum, etc.) estimated using landslide models (Hibert et al., 2014, 2011; Levy et al., 2015) or from inversion of low-frequency seismic data (Hibert, Ekström, & Stark, 2017). In particular, Hibert, Ekström, and Stark (2017) observed that the flow momentum is generally proportional to the amplitude of the high-frequency envelope of the signal. However, sometimes, in particular during the deceleration phases, a high-frequency signal can be observed even if the force inverted from the seismic signal, which is proportional to the landslide acceleration, is almost zero, leading to an apparent zero-velocity (see gray area in Figure 1). Even nonaccelerating, constant-velocity flows generate seismic waves, possibly due to grain agitation. The generation of high-frequency signals by agitated flowing grains has been both observed and theorized. Huang et al. (2007) compared the high-frequency seismic signals generated by rock impacts and debris flows (grain/fluid mixtures) and concluded that one of the main sources of ground vibration caused by debris flows is the interaction of rocks or boulders with the channel bed. Models for this process have been both developed and tested, by Farin, Tsai, et al. (2019), Kean et al. (2015), Lai et al. (2018), and Zhang et al. (2021). However, the complexity of natural landslides and the difficulty of obtaining accurate measurements

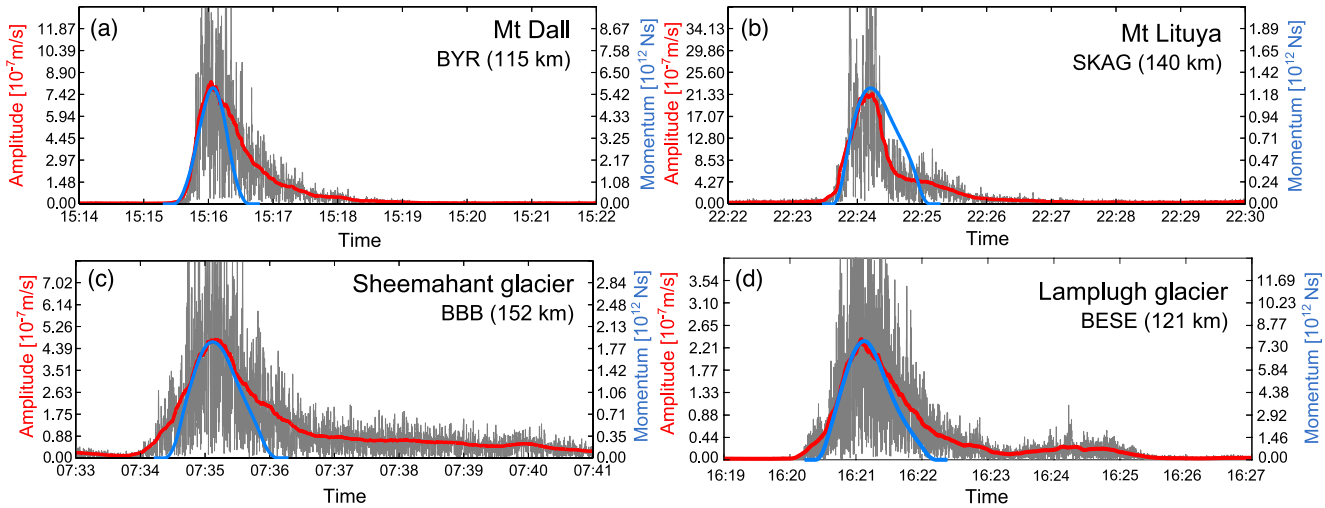

Figure 1. Seismic signal envelope (gray), smoothed envelope (red), and inverted momentum (blue) from the inversion method proposed by Ekström and Stark (2013) for landslides on (a) Mt Dall, (b) Mt Lituya, (c) the Sheemahant glacier and (d) the Lamplugh glacier, as a function of time (UTC, Hour:min format), with the second line of each legend indicating the seismic station and its distance from the landslide.

of their dynamics makes it nearly impossible to quantify, or rigorously test models of, the link between grain-scale physical processes, such as velocity fluctuations, and the generated seismic signal. More generally, the measurement of particle agitation, called granular temperature in the kinetic theory of granular flows, and its link with mean flow properties in dense flows are still open questions, closely related to the rheology of granular materials (see for example, Andreotti et al., 2013; Delannay et al., 2017 for review papers).

A few studies addressed this issue with laboratory scale experiments, recording and quantifying the seismic (i.e., acoustic) waves generated by almost steady and uniform granular flows. These experiments make it possible to test physical interpretations of the characteristics of the seismic signal generated by natural landslides and to quantify the partition of energy between the flow and its seismic emissions. Furthermore, such experiments provide a unique way to check models of granular flows and seismic wave generation in a simple configuration, before tackling natural applications.

In model granular layers, Aleshin et al. (2007) have theoretically investigated guided modes of mechanical waves and shown the existence of a property gradient due to gravity. This was experimentally evidenced at laboratory scale by Jacob et al. (2008) and Bonneau et al. (2008). Zaitsev, Gusev, et al. (2008) and Zaitsev, Richard, et al. (2008) have evidenced acoustic emissions precursory to granular flow and used acoustic probing of granular layer changes in the context of granular avalanches at the laboratory scale. Acoustic emissions during granular shear have also been investigated by Michlmayr et al. (2013). de Richter et al. (2010) and Zaitsev et al. (2014) have demonstrated the slow evolution and ageing of acoustic properties during the restoration of contacts in granular packings.

In a 8-m long channel, Huang et al. (2004) investigated the acoustic waves generated by (a) the friction and impacts of rocks of about 100 g to 1 kg on a granular bed filled with water and slurry and (b) debris flows of gravel and water/slurry. They recorded similar frequencies for individual rock motion and debris flows, as observed in the field by Huang et al. (2007). Their measurements also showed that the amplitude of the acoustic signal increases with gravel size. However, as with the later, better-instrumented experiments of de Haas et al. (2021) on debris flows of clay, sand, gravel, and water, the complexity of the materials involved and the lack of measurements at the grain scale made it difficult to capture the origin of the generated signal and to quantify the link between the acoustic measurements and the flow properties.

Working with more monodisperse grains, researchers investigating "booming dunes" have recorded acoustic signals that are generated by grain agitation but differ from those of landslides in being coherent. The reviews of Hunt and Vriend (2010) and Andreotti (2004, 2012) present different perspectives on experiments and field observations, agreeing that internal shear generates initial signals with frequency related to the shear rate but without consensus on the mechanism by which certain dune sands produce clear tones of around 100 Hz. In

sheared and confined granular layers of similarly monodisperse grains, wave propagation through the granular structure has been investigated by Lherminier et al. (2014).

Shearing similarly well-sorted beach sands in a torsional rheometer, Taylor and Brodsky (2017) found that the square of the acceleration measured with their accelerometers divided by the number of particles was proportional to $I \times d^3$, where d is the particle diameter and I the so-called inertial number, defined as the ratio between the timescale related to shear and the timescale related to particle rearrangement under confining pressure. However, Taylor & Brodsky (2017) neither calculated absolute values of the acoustic energy nor measured the characteristics of the flow such as velocity fluctuations, mean velocity profiles, etc.

A series of experiments on granular impacts on various smooth beds showed that Hertz theory quantitatively explains the acoustic signal generated in the bed substrate (Farin et al., 2015). These experiments also showed that power laws issued from this theory make it possible to empirically relate the acoustic energy to the properties of the impactor (mass and velocity) on smooth, rough, and erodible beds (Bachelet et al., 2018; Farin et al., 2016, 2015). More specifically, the characteristic frequency of the acoustic signal is shown to decrease with increasing impactor mass and to increase with increasing impact velocity, while the radiated energy of the acoustic signal increases with both increasing mass and increasing velocity, as observed for debris flows (Okuda et al., 1980) and for single block rockfalls (Hibert, Malet, et al., 2017). These quantitative relationships, between acoustic and kinematic properties, were discovered thanks to accurate measurement and calculation both of grain motion and of the absolute value of radiated acoustic energy, using coupled optical and acoustic methods.

With similar methods, Farin et al. (2018), Farin, Mangeney, et al. (2019), and Farin, Tsai, et al. (2019) showed that during 3D granular collapses on inclined planes, the rate of seismic energy emission varies in the same manner as the flow velocity. In particular, analyzing the period of flow that follows grains' initial acceleration and deceleration, the rate of seismic energy emission increases with increasing slope, as do the downslope velocity and the agitation of particles at the flow front. However, grain-scale fluctuations were not measured.

The acoustic signals of flows that are comparably energetic, but steady and apparently uniform, were investigated by Arran et al. (2021), which used carefully calibrated force and flux measurements, high-speed photography, and accelerometer recordings to test the models of Farin, Tsai, et al. (2019), Kean et al. (2015), Lai et al. (2018). With the flows' bulk inertial numbers I between 0.1 and 5 and indications of basal slip, acoustic signals were best predicted by a model adapted from Farin, Tsai, et al. (2019), in which signals are generated by Hertzian impacts, with the ground, of particles with mean velocity equal to that of the flow. But this prompts a new question: how are signals generated by less energetic flows, in which basal particles are almost static and the collisions of other particles, far from the flow's base, will be more significant?

We investigate here the quantitative link between velocity fluctuations, mean flow properties, and acoustic energy by combining accurate optical and acoustic measurements of granular flows over a range of slopes. Compared to Arran et al. (2021), we focus here on more gentle slopes, on which flows are almost steady and uniform but a persistent contact network links almost static basal particles to energetic particles far from the base. Our objectives are to (a) capture and quantify the fluctuations and heterogeneities in almost steady uniform flows and their relationship with mean flow properties, (b) characterize and quantify the radiated acoustic energy, (c) relate the acoustic characteristics (energy, frequency) to the grain-scale and mean properties of the flow, (d) check whether a simple model based on particle collisions at fluctuating velocities can quantitatively explain the measured seismic power, (e) quantify the relative contributions of collisions within the flow and with the bed on the generated acoustic energy, (f) quantify the proportion of energy lost by vibrations, and (g) discuss our results with regards to field observations.

2. Setup

The experimental setup consists of a 1.5 m long chute made of poly(methyl methacrylate) (PMMA), inclined at an angle θ to the horizontal, with rigid side walls 10 cm apart. Granular flows are initiated by opening a gate that releases glass particles of diameter $d = 2$ mm and density $\rho = 2{,}500$ kg m^{-3}, initially stored in a tank (Figure 2). The rough bed is made of the same glass particles, glued to the PMMA plate with phenyl salicylate, a crystalline substance with low melting point. As opposed to tape, it prevents the glued particles from vibrating and significantly disturbing the acoustic signal. The two control parameters are the height of the gate h_g and the slope angle of the channel θ, which varies between $\theta = 16.5°$ and $\theta = 18.1°$. Note that the

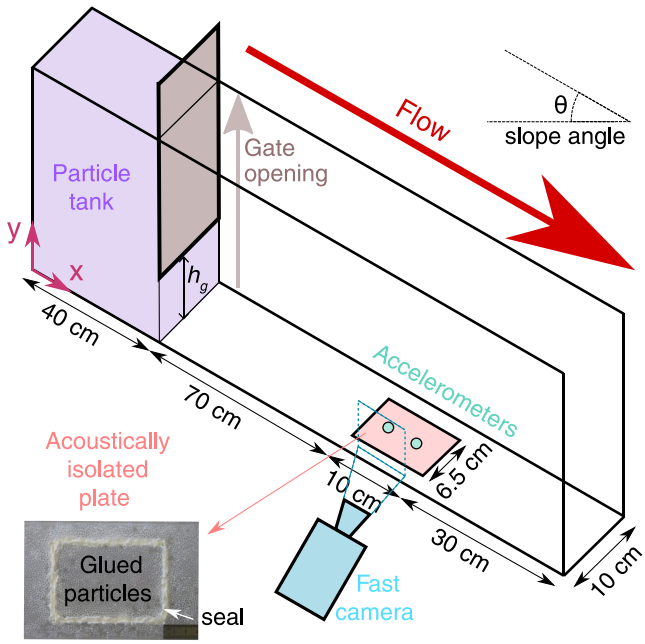

Figure 2. Setup, composed of a narrow inclined channel in which granular flows are created by opening the gate of the upstream tank that contains glass particles. The same particles are glued to the bottom plate to obtain a rough surface. The flow properties are measured using a high-speed camera and the generated acoustic waves by accelerometers fixed on the channel bottom.

flow thickness is related but not equal to the height of the gate, which varies between $h_g = 4.4$ cm and $h_g = 8.5$ cm. In this range of inclination angles, almost steady and uniform flows can be observed at about 70 cm from the gate (as discussed below). The characteristics of these flows are summarized in Table 1. 70 cm from the gate, a Photron SA5® high-speed camera (5,000 frames per second) records the flow during 2 s with a field of view of around 50 mm by 50 mm. Simultaneously, two accelerometers (Bruel & Kjaer, 8309, bandwidth 10 Hz–54 kHz) record the radiated acoustic waves. These accelerometers are glued, using the same phenyl salicylate as for the particles of the rough surface, on the back of a $L \times l = 10$ cm $\times$ 6.4 cm plate, isolated acoustically from the rest of the channel bottom. To isolate the plate, we fixed it to the channel bottom with a silicone sealant (see bottom of Figure 2).

3. Optical and Acoustic Methods

Our objective is to obtain deep quantitative insights into the mean properties of the flow and into its fluctuations and heterogeneity, in order to further interpret the generated acoustic signal in terms of grain scale and mean flow dynamics. Before analysis of these measurements, in Section 4, let us detail below the optical and acoustic methods used here to measure flow and acoustic characteristics, respectively. To illustrate the methods, we focus in this section on the two "extreme" cases representing the slower flows by experiments 1 and 2, at $\theta = 16.5°$, with flow thicknesses $h = 3.5$ cm and $h = 3.6$ cm and surface velocities $V_{xs} = 0.30$ m s^{-1} and $V_{xs} = 0.29$ m s^{-1}, and the faster flows by experiment 9 at $\theta = 18.1°$, with $h = 3.3$ cm and $V_{xs} = 0.48$ m s^{-1} (Table 1).

3.1. Flow Measurement Using Optical Methods

The flows in all our experiments reach an almost steady and uniform regime: their heights typically vary by one particle diameter or less in space and time over the entire recorded experiment (see Figure A1 in the Appendix). The flow is steady over the central half of the experiment, up to statistical fluctuations. From the average height decrease between $x = 0$ and $x = 25d = 50$ mm (Figure A1 c in the Appendix), a variation from uniformity of 1° can be estimated: the slope angle is slightly below that required to maintain a steady, uniform flow, and steadiness is maintained by net energy input from the grains' initial release.

Table 1
Parameters of the Quasi-Steady and Quasi-Uniform Flows Obtained in Our 9 Experiments (Referred to by the Index 1–9): Slope Angle of the Channel θ, Thickness of the Flow h, Downslope Velocity of the Surface Particles V_{xs}, Depth- and Time-Averaged Downslope Velocity $\langle\langle V_x\rangle\rangle$, Shear Rate $\langle\dot{\gamma}\rangle$, and Inertial Number $\langle I\rangle$

Index	θ [°] (±0.1)	h/d (±0.5)	$V_{xs}/\sqrt{gd}$ (±0.05)	$\langle\langle V_x\rangle\rangle/\sqrt{gd}$ (±0.05)	$\sqrt{d/g}\,\langle\dot{\gamma}\rangle$ (±0.01)	$\langle I\rangle$ (±0.003)
1	16.5	17.5	2.15	0.65	0.12	0.070
2	16.5	18.0	2.05	0.55	0.10	0.054
3	16.5	20.0	2.35	0.80	0.12	0.061
4	17.2	15.5	2.50	0.75	0.15	0.094
5	17.2	16.5	2.85	0.90	0.16	0.094
6	17.2	16.5	2.95	1.00	0.17	0.103
7	18.1	14.5	2.02	0.50	0.11	0.074
8	18.1	15.0	2.95	0.90	0.18	0.103
9	18.1	16.5	3.45	1.10	0.21	0.131

Note. Note that here $d = 2$ mm, $\sqrt{gd} \simeq 0.14$ m/s, and $\sqrt{d/g} \simeq 0.014$ s.

3.1.1. Mean Velocity and Fluctuations

We measured particle velocities $\mathbf{V} = (V_x, V_y)$ by Correlation Image Velocimetry (CIV) and Particle Tracking Velocimetry (PTV). CIV divides each image from the high-speed camera into boxes and calculates the average displacement into each box by correlation of the graymap between successive images (Figure 3a). The size of the boxes is a crucial parameter. Boxes that are too large miss individual particles whereas boxes that are too narrow do not allow good correlations. Similarly to Gollin et al. (2015a), the size of the boxes was chosen to be equal to 1.14 particles. The overlap between boxes is 75%. We used the code developed by Thielicke and Stamhuis (2014).

On the other hand, PTV detects and follows the particle positions, making it possible to record their trajectories (Figure 3b). The particles are semitransparent and cause complex reflection effects. Consequently, a compromise must be made between the completeness and accuracy of detections. PTV shows that particles are essentially organized into layers that do not really mix during the flow. Mean velocities $\langle \mathbf{V} \rangle = (\langle V_x \rangle, \langle V_y \rangle)$ are therefore calculated by averaging the measurements within each layer (over 1 particle diameter in the y-direction), the borders of which are clearly visible on the PTV images (Figure 3b). As done for calculating the mean thickness, the averaging is performed over about 16 particles in space in the downslope direction and over the whole experiment duration (2 s).

Velocity fluctuations δV are computed over the same intervals (2 s, 16 particles in the x-direction and 1 particle in the y-direction) by taking the standard deviation of the norm of the velocities:

$$\delta V = \sqrt{\delta {V_x}^2 + \delta {V_y}^2}, \tag{1}$$

where $\delta V_i^2 = \left\langle (V_i - \langle V_i \rangle)^2 \right\rangle$ the variance of the velocity along the i-direction, with $i = x, y$. For granular systems, the measurement of velocity fluctuations may lead to scale dependency effects due to gradients developing in the flow (see e.g., Artoni & Richard, 2015a, 2015b). Indeed, the thickness w of the layers within which the velocity fluctuations are calculated affects the estimates. Following Glasser and Goldhirsch (2001), we showed that the size dependency starts for $w > 2$d (see Figure B1 of Appendix B). In the following, we will consider velocity fluctuations calculated with a window size $w = d$. Note that when velocity fluctuations are calculated with a smaller averaging window (e.g., $w = 0.2$ d), the layering of the flow clearly appears and resembles that observed by Weinhart et al. (2013) (Figure B1, Appendix B). Note also that velocity fluctuations of about $0.1\sqrt{gd}$ are measured near the bottom, where the mean velocity is zero. This indicates the order of magnitude of the error in the measurement of velocity fluctuations ($\sim$0.01 m s^{-1}).

The profiles of mean velocity, in both the downslope ($\langle V_x \rangle$) and normal ($\langle V_y \rangle$) directions, differ by at most 10% when obtained using CIV as compared to PTV, as illustrated in Figure 3c. In contrast, velocity fluctuations may differ by up to a factor of two between the two methods. This discrepancy has also been observed by Gollin et al. (2015b) and Gollin et al. (2017) and seems to be due to the average nature of CIV, which is therefore less suitable to measure fluctuations. As a result, PTV measurements will be used in the following, as in Pouliquen (2004), except for mapping of the spatiotemporal distribution of velocity fluctuations (Figure C1).

3.1.2. Packing Volume Fraction

The setup can only measure the surface packing fraction ϕ_{2D} at the lateral walls (Fig. 3de), with specular reflections making it impossible to apply Sarno et al. (2016)'s method for estimating the (typically smaller) volume packing fraction. Furthermore, one observes an ordering of the particles along the walls, with a close to hexagonal pattern visible in Figure 3d. Nevertheless, one expects qualitative variations with depth of the 2D volume fraction along the walls to reflect the qualitative behavior in the volume; as is typically observed, we measure an almost constant packing fraction within the flow and a decrease when approaching the free surface (Figure 3e). Due to the strong uncertainty in our measurements, the change of ϕ_{2D} when increasing the slope angle (i.e., when the inertial number changes) is hard to capture, even though a decrease of ϕ_{2D} with increasing inertial number is visible near the surface, in agreement with the literature (GDR MiDi, 2004). Calculation of the volume fraction shows the layering of the granular flows observed, for example, by Artoni and Richard (2015b) and Weinhart et al. (2013).

3.1.3. Frequency of Particle Oscillations

During the flow, vertical oscillations of the particles can be observed, related to compression/dilatation effects occurring when one layer passes over another (see Movies S1 and S2 in Supporting Information S1). These

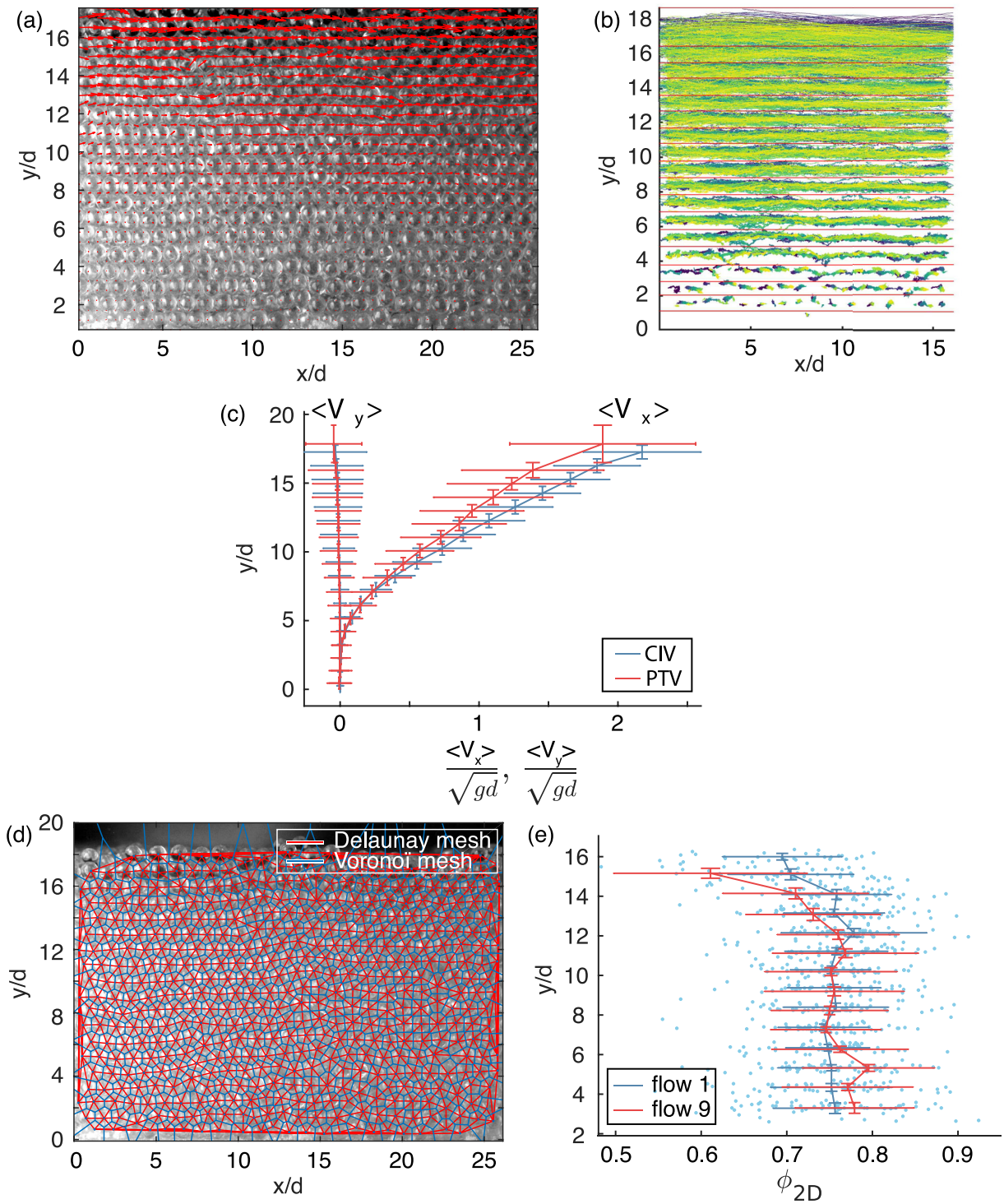

Figure 3. Examples, from experiment 2, of image analysis. (a) A velocity field calculated by Correlation Image Velocimetry (CIV) (red arrows) and (b) a superposition of particle trajectories, over 2 s, obtained with Particle Tracking Velocimetry (PTV). The organization of the flow into a superposition of layers is clearly visible. In (b), red lines indicate the separation between layers. (c) Mean downslope and normal velocity profiles $\langle V_x \rangle$ and $\langle V_y \rangle$, as a function of the position above the bottom y. The associated velocity fluctuations are represented by the horizontal error bars. Vertical error bars correspond to the thickness of the layer within which the velocity has been averaged. One can compare the measurements made by CIV (blue line) and PTV (red line). (d and e) Surface packing fraction of the particles in contact with the lateral wall: (d) manual picking of the particles of flow experiment 1 in Table 1 ($\theta = 16.5°$, $h/d = 17.5$, i.e., $h = 35$ mm) at one instant and (e) the inferred surface packing fraction (blue dot) per Voronoï cell, Φ_{2D} obtained by projecting spheres as disks on the wall. The average values are plotted in the solid blue line. For comparison, the average surface packing fractions of flow experiment 9 in Table 1 ($\theta = 18.1°$, $h/d = 16.5$, i.e., $h = 33$ mm) are plotted with the solid red line.

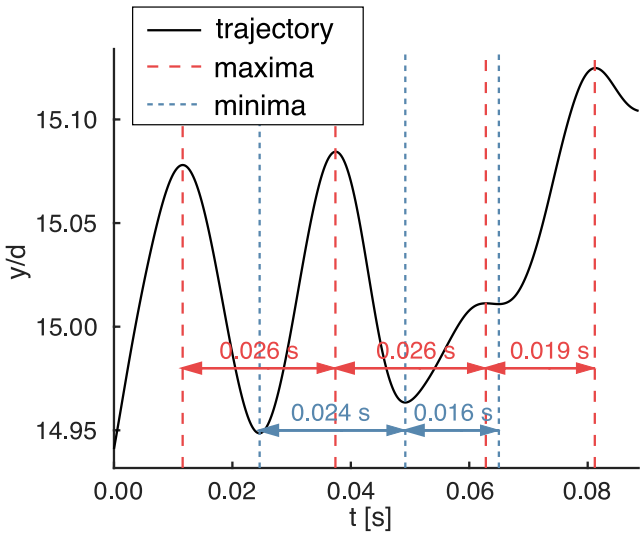

Figure 4. Example (from experiment 2) of vertical particle oscillations captured by Particle Tracking Velocimetry, for a particle located close to the surface of the flow: The smoothed trajectory demonstrates the calculation of the average period of the oscillations $\tau \simeq 0.02$ s.

oscillations are captured in PTV measurements of the trajectories of particles located at the surface (Figure 4). Indeed, several oscillations can be observed before these particles' relatively high velocity causes their tracking to fail. On the contrary, for particles located deeper in the flow, oscillations generally occur when tracking has already failed. For oscillations that are captured, the oscillation frequency f_{osc} is calculated by filtering each particle trajectory with two filters and taking the median of values $1/\tau_i$, where each $\tau_i \simeq 0.02$ s is the time between successive maxima or minima of each filtered trajectory (Figure 4). More precisely, the first filter is a normalized median filter adapted from Westerweel & Scarano (2005) and applied to each trajectory component, with a neighborhood radius of 5 successive positions, an acceptable fluctuation level of $\varepsilon = 0.10$ pixels and a detection threshold equal to the median difference between particles' velocities and the median of velocities in their local neighborhood (for technical details, see Westerweel & Scarano (2005)). The second filter is a second order zero-phase low pass filter (cutoff frequency of 50 Hz). The median filter has been chosen to suppress random fluctuations.

3.2. Elastic Wave Measurements

The elastic waves generated by the granular flows and by their interactions with the bottom are recorded by two accelerometers glued to the isolated plate (Figure 5a). It is assumed here that the accelerometers mainly record the vibrations generated by the section of granular flow over the plate. Isolation of the plate from the rest of the flume was verified by comparing the signals recorded by accelerometers glued to these two elements (Bachelet, 2018).

3.2.1. Radiated Elastic Power

The average radiated elastic power over duration Δt is $\Pi_{el} = W_{el}/\Delta t$, where W_{el} is the radiated elastic energy. The acoustically isolated plate is small compared to the characteristic viscoelastic attenuation length of energy in PMMA. As a result, elastic waves are reflected many times at the boundaries of the plate, leading to a diffuse elastic field, that is, a situation in which energy can be assumed to be homogeneously distributed over the plate and equipartitioned. The elastic energy dissipated over Δt can then be approximated from measurements of plate-normal velocity v_z, by using the diffuse field theory proposed by Farin et al. (2016):

$$W_{el} = M\,\gamma_p\,v_g \times \int_{\Delta t} v_z^2(t)\mathrm{d}t, \tag{2}$$

where $M \simeq 80$ g is the mass of the isolated piece of plate, $\gamma_p \simeq 3$ m^{-1} its average viscoelastic attenuation, and $v_g \simeq 1{,}000$ m s^{-1} the average group velocity of the radiated acoustic waves (A_0 Lamb waves). The value of γ_p is obtained by measuring the response of the plate at various distances with a source and a vibrometer and the value of v_g by calculating the dispersion relation of the A_0 Lamb modes of the plate, following Royer & Dieulesaint (2000) (Bachelet, 2018). The measurements to determine γ_p were performed on a PMMA plate of size 1 m by 1 m, with material and thickness corresponding to the isolated piece of plate. The amplitude at first passage of a wave induced by a piezoelectric sensor was measured with the vibrometer at distances up to 60 cm from the source, every mm. The source was excited by a 1 s-long chirp (or sweep) with an instantaneous frequency linearly increasing from 1 to 50 kHz. This permitted determination of the dispersion relationship and the attenuation of the A_0 mode in both the 1 m by 1 m plate and the experimental isolated plate. A large time window $\Delta t = 0.2$ s is selected in order to consider only slow changes of Π_{el}. The fast fluctuations will be characterized in the next section. An example of radiated elastic power computation is presented in Figure 5a.

3.2.2. Frequency Content

The spectrograms shown in Figures 5f and 5g indicate that the main frequency content of the acoustic signals lies between 20 and 30 kHz. Amplitude spectra are not studied beyond 54 kHz, which is the upper limit of the accelerometers' flat response. This prevents us from reliably measuring the mean frequencies of the seismic signals.

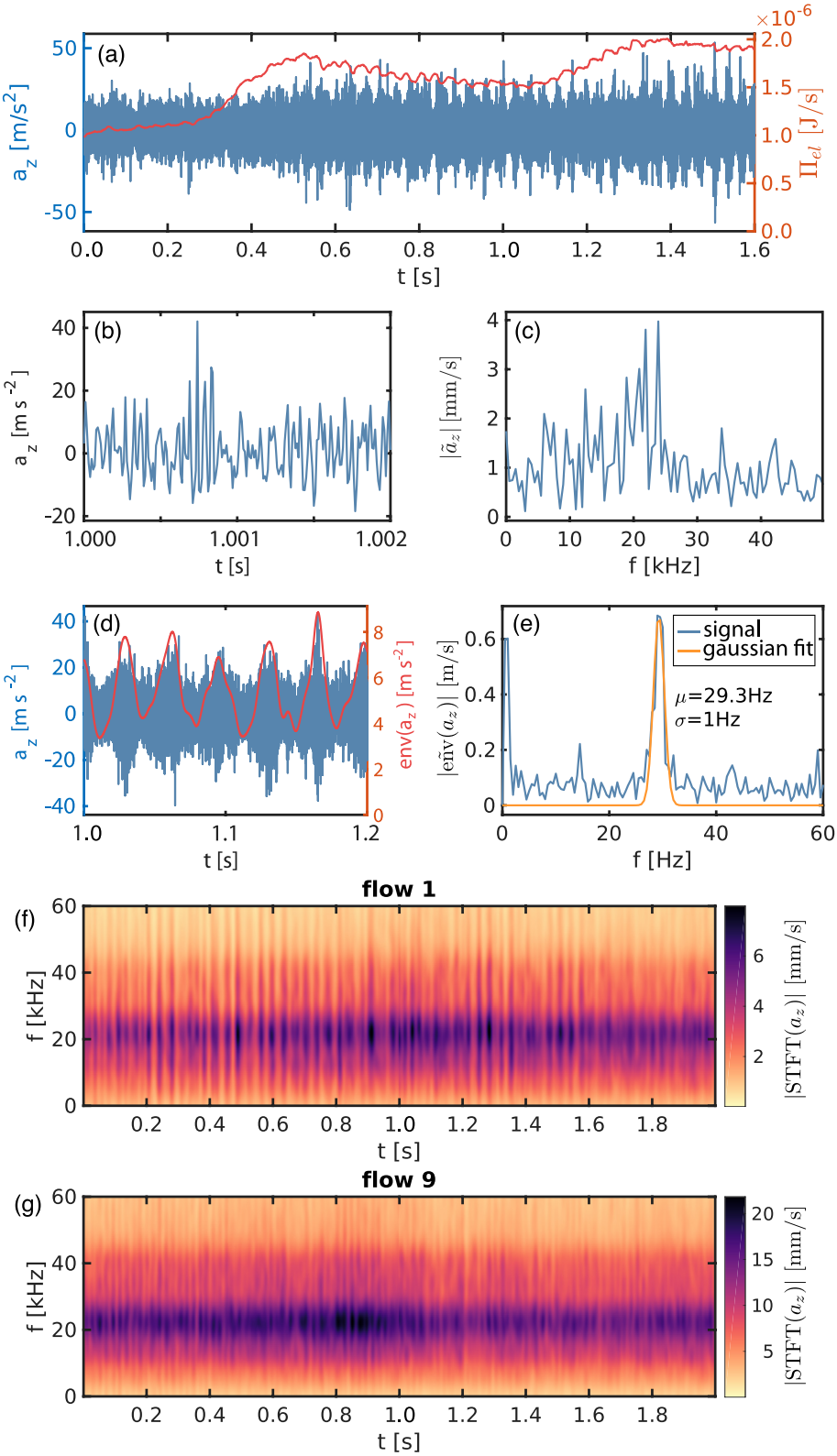

Figure 5. Acoustic signal of flow number 2: (a) acceleration of the vibration (blue) and associated elastic power (red), (b) an excerpt of the acoustic signal and (c) its frequency spectrum, (d) envelope (red) of the acoustic signal (blue) and (e) the frequency spectrum of this envelope. (f and g) Spectrograms of the signal of experiment 1 ((f), $\theta = 16.5°$, $h = 3.5$ cm, $V_{xs} = 0.30$ m s^{-1}) and experiment 9 ((g), $\theta = 18.1°$, $h = 3.3$ cm, $V_{xs} = 0.48$ m s^{-1}).

Vertical stripes can be identified on the spectrograms (Figures 5f and 5g). The time interval between these stripes decreases as the slope angle increases. The frequency content of this amplitude modulation is between 25 and 50 Hz, that is, about 1,000 times smaller than the highest frequencies at which we detect signals. To calculate the modulation frequency f_{mod}, we first extract the envelope of the signal (the absolute value of its analytic representation) and apply a low pass filter (cutoff frequency empirically fixed at 75 Hz). Then, the modulation frequency is determined by fitting a Gaussian in Fourier space (Figures 5d and 5e).

4. Flow Characteristics

Our objective here is to capture the relationship between mean flow properties and the fluctuations that are expected to play a role in acoustic emissions. Note that the flow measurements are made at the side walls. It is well known that the wall boundaries significantly affect the mean flow quantities and their fluctuations, as will be discussed below (see e.g., Artoni & Richard, 2015b; Fernández-Nieto et al., 2018; Jop et al., 2005, 2007; Mandal & Khakhar, 2017; Taberlet et al., 2003).

4.1. Mean Flow

The nearly uniform and steady flows obtained here, confined in a narrow channel inclined at slope angles between 16.5° and 18.1°, are similar to those observed by Hanes & Walton (2000) in similar settings. In these flows, the mean downslope velocity $\langle V_x \rangle(y)$ is maximized at the free surface, decreasing down to zero near the bottom (Figure 6). Such convex velocity profiles are observed in flows confined in narrow channels (see e.g., Ancey, 2001; Courrech du Pont et al., 2003; Jop et al., 2005, 2007; Mandal & Khakhar, 2017; GDR MiDi, 2004; Taberlet et al., 2003) and differ from the Bagnold-like velocity profiles obtained for steady and uniform flows in wide channels (see GDR MiDi (2004) or Figure 4 of Fernández-Nieto et al. (2018)). These profiles have a shape that can be approximately fitted by the velocity profiles assumed in Josserand et al. (2004) to describe heap flows:

$$1 - \frac{\langle V_x^J \rangle(y')}{\langle V_x \rangle(y'=0)} = \left(\frac{1 - e^{-y'/Y}}{1 + \left(\frac{\phi_M}{\phi_m} - 1 \right) e^{-y'/Y}} \right)^{3/2}, \tag{3}$$

where $y' = h - y$ and h is the height of the flow surface, Y is a fitting parameter, and $\phi_m = 0.5$ and $\phi_M = 0.65$ are the loose and dense random packing fraction, respectively. Figure 6 shows that Equation 3 fits our experimental data quite well, except near the bottom for experiments with thick flow depth h, for which the horizontal velocity is nonzero at the base. While second order polynomials ($\langle V_x \rangle / \sqrt{gd} = a^*(y/d)^2 + b^*(y/d)$) give even better results, especially near the bottom, we use the physically motivated fits of Equation 3 to calculate the shear strain rate $\dot{\gamma} = \partial \langle V_x^J \rangle / \partial y$. We do not calculate γ for the surficial layer, which is poorly modeled by dense, continuum shear.

The shear strain rate $\dot{\gamma}$ decreases from the surface down to the bottom (Figure 7b). Granular flows are characterized by the inertial number $I = \dot{\gamma} d / \sqrt{P/\rho}$, where ρ is the grain density and P the pressure, taken here to be hydrostatic ($P = \rho \phi g \cos(\theta)\,(h - y)$):

$$I(y) = \frac{\dot{\gamma}(y) d}{\sqrt{\phi g \cos(\theta)(h - y)}}. \tag{4}$$

The packing fraction is approximated by $\phi = 0.6$ (Jop et al., 2005) because we do not have access to the packing fraction in the bulk of the flow (see Section 3.1.2). As the velocity profiles are not Bagnold-like, the inertial number is not constant with depth here but decreases from the surface to the bottom (Figure 7c).

4.2. Velocity Fluctuations

The high-frequency acoustic signal generated by granular flows is expected to arise mainly from particle collisions, as indicated by Huang et al. (2007), though other effects may play a role (Michlmayr et al., 2013). Squeal noise associated with friction in granular media has been documented by Akay (2002) but, in the unconfined configuration of free surface granular flow, we hypothesize that normal forces between the centers of colliding

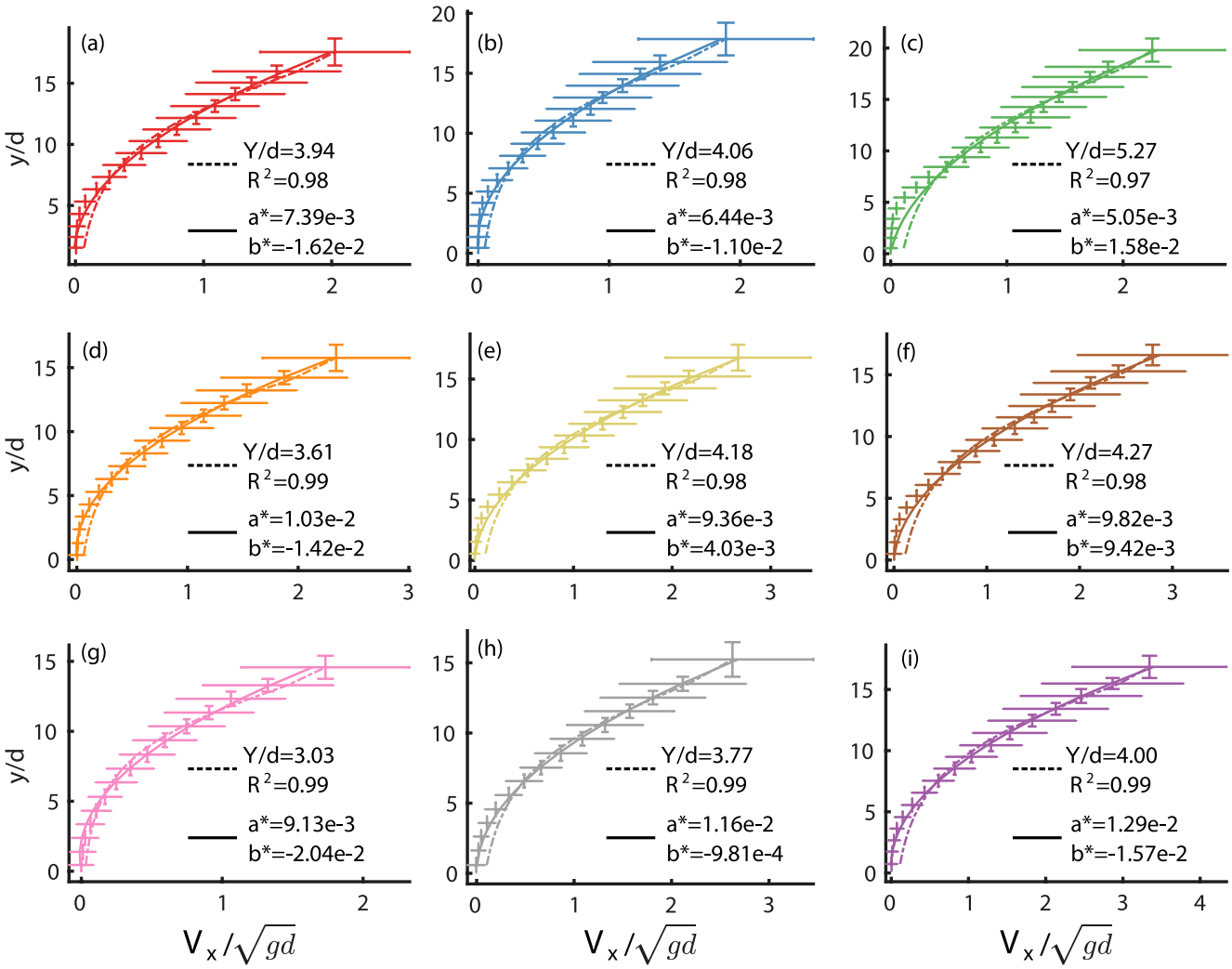

Figure 6. Velocity profiles of all the experiments, with letters (a) to (i) referring to flows 1 to 9, corresponding to the angles (a–c) $\theta = 16.5°$, (d–f) $\theta = 17.2°$, and (g–i) $\theta = 18.1°$ and to increasing flow thickness along each row (see Table 1 for details). Two theoretical profiles have been fitted: the ones given by Equation 3 in dashed lines and a second order polynomial ($\langle V_x \rangle / \sqrt{gd} = a^*(y/d)^2 + b^*(y/d)$) in solid lines. For all polynomial fits, $R^2 \geq 0.99$.

grains are larger than the sliding forces between surfaces of grains in contact, so we focus on the normal component of collisions. Such collisions occur only when neighboring particles have different velocities, either due to a gradient of mean velocity or as a result of fluctuations about their mean velocities.

Velocity fluctuations, quantified by their mean squared values (the "granular temperature") (Goldhirsch, 2008)

$$T = \delta V^2, \tag{5}$$

are known to be significant in granular flows. In general, however, granular temperature is not explicitly accounted for in the rheology of dense granular flows, except in the extended kinetic theory (for example, Berzi, 2014; Gollin et al., 2017). Indeed, the relationship between velocity fluctuations and the inertial number or other mean flow quantities has not yet been thoroughly investigated in dense granular flows. They are difficult to measure experimentally and even more so in the field (Berzi & Jenkins, 2011; Hill & Tan, 2014). The acoustic power, which is much easier to measure, may provide a unique tool to obtain quantitative measurements of granular temperature, as will be investigated below.

Figure 7a shows that measured velocity fluctuations decrease from the surface to the bottom for all experiments and increase with slope angle. Using discrete element modeling, Hanes and Walton (2000) showed that the granular temperature profile is very different at the side wall than it is within the core of the flow: the simulated

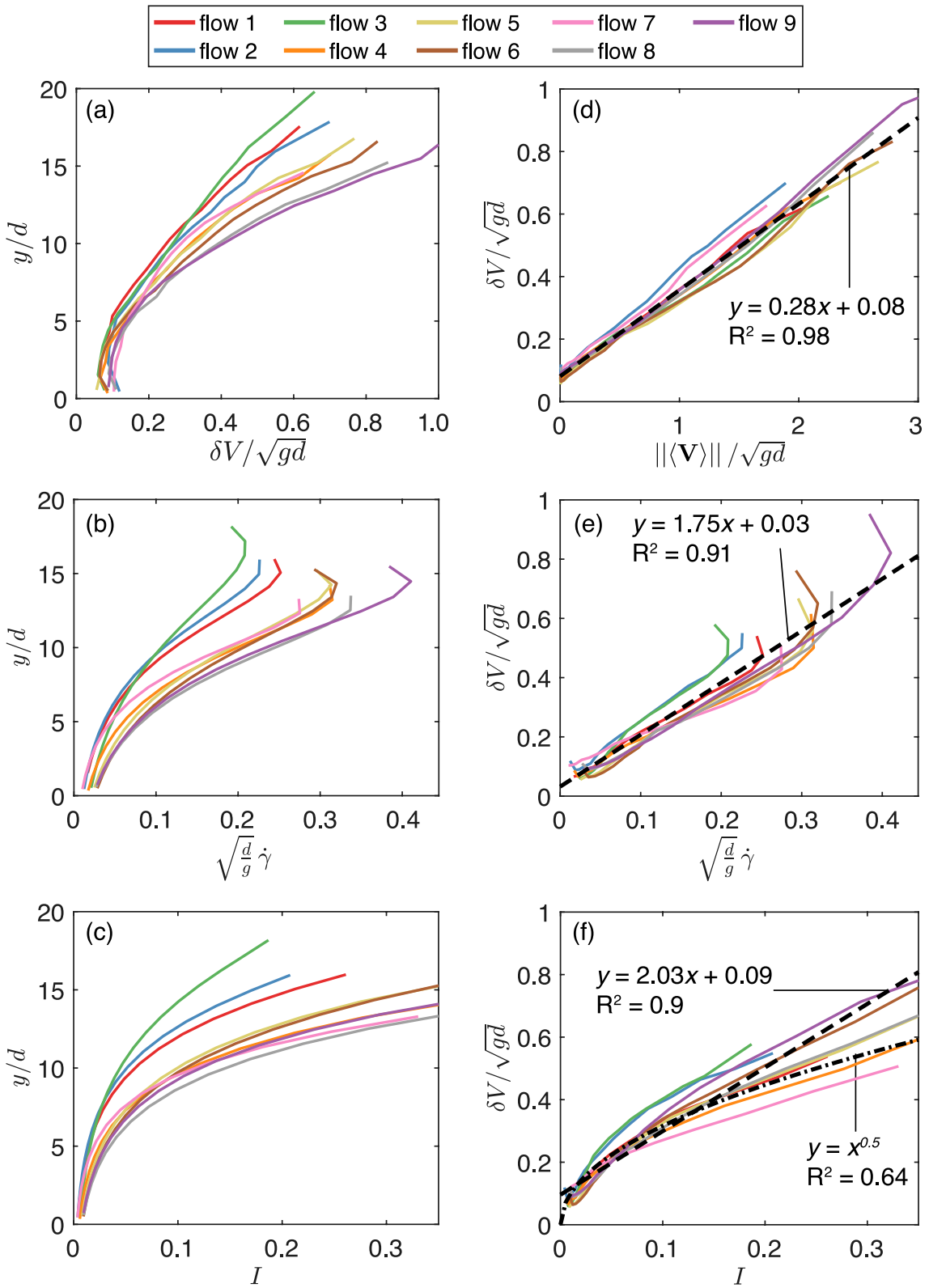

Figure 7. (a) Normalized fluctuating speed $\delta V/\sqrt{gd}$ (with $\sqrt{gd} \simeq 0.14$ m/s), (b) normalized shear rate $\sqrt{d/g}\dot{\gamma}$ (with $\sqrt{d/g} \simeq 0.014$ s), and (c) inertial number I, computed using the second order polynomials that provide the best fit to $\langle V_x \rangle$, as functions of flow depth y/d, for all of the experiments (colors). (d) to (f) Normalized fluctuating speed $\delta V/\sqrt{gd}$ as a function of (d) the mean flow speed $\|\langle \mathbf{V} \rangle\|/\sqrt{gd}$, (e) the normalized shear rate $\sqrt{d/g}\dot{\gamma}$, and (f) inertial number I. In panels (d) to (f), dashed lines show fits of the data with linear laws. In panel (f), the dash-dotted line shows a power-law (square root) fit of the data.

granular temperature is, at the surface, the same at the side walls and across the flow, but increases with depth in the middle of the flow while decreasing with depth at the side walls, as observed in these experiments.

Even though velocity fluctuations about the mean look regular when averaged over volume and time, Figures C1a and C1b in the Appendix and Movies S3 and S4 in the Supporting Information S1 illustrate the existence of transient vortices of velocity fluctuations in our experiments, as observed by Kharel and Rognon (2017). The size and intensity of these transient vortices seem to be related to the flow regime, leading to strong variation of velocity fluctuations (in space and time) where the flow is close to jamming, possibly contributing to acoustic emissions from these regions. The correlation length of these velocity fluctuations is around 1 grain diameter in the y-direction and can reach up to 8d in the x-direction, decreasing with increasing slope (see Figure C2 in Appendix C).

4.3. Relationship Between Mean Properties and Fluctuations

Granular temperature is expected to scale with the square of the shear strain rate, so that $\delta V \propto \dot{\gamma}$ (see for example, Andreotti et al., 2013; Pouliquen, 2004). Such a linear relationship between δV and $\dot{\gamma}$ seems indeed to be satisfied (Figure 7e), in very good agreement with observations at the surface of granular flows by Pouliquen (2004) and in other configurations (GDR MiDi, 2004). If we try to fit the data by a power law, we get a power equal to 2 with high R^2. A higher R^2 is found when trying to relate the velocity fluctuations to the mean downslope velocity $\langle V_x \rangle$ (Figure 7d). The slightly higher R^2 may result from errors in the estimation of the gradient of the measured velocity profile. Any power law relationship between velocity fluctuations and the inertial number is less clear, with a smaller R^2 (Figure 7f). This could, similarly, be due to the errors in the calculation of I. As a result, velocity fluctuations averaged in time and along one layer of grains scale very well with shear rate and with mean velocity and to a lesser extent with the inertial number:

$$\delta V \propto \langle V_x \rangle \propto \dot{\gamma} \propto I^{0.5}. \tag{6}$$

5. Signature of Flow Dynamics in the Acoustic Signal

Our objective is to quantitatively relate the characteristics of the seismic signal to those of the flow, in order to (a) get physical insights into the sources of acoustic emission and (b) propose empirical scaling laws that can be used to recover flow properties from the recorded acoustic waves. As the range of configurations (slope angle and thickness) investigated here is not very large, it is hard to discriminate between power laws or linear trends. We will therefore systematically test these two types of empirical fits and quantify the associated R^2.

5.1. Acoustic Frequencies

5.1.1. Orders of Magnitude of Possible Signal Frequencies

Let us first discuss the orders of magnitude of the signal frequencies that the physics of the granular flow could generate, based on our setup and on the observation of flow dynamics described in the previous sections. We have identified six physical processes that present different frequency signatures.

The frequency range of the signal is expected to be determined by the physics of a typical interparticle collision, scaling with the inverse of the Hertzian contact time between two spheres of diameter d that have collided at relative velocity δV (Farin et al., 2015). For impacts between such particles, Bachelet (2018) proposed the following expression for the amplitude-weighted mean signal frequency:

$$f_{Hertz} = a'_0 \, d^{-1} \, \delta V^{1/5}, \tag{7}$$

where

$$a'_0 \simeq 0.90 \left(\frac{E\sqrt{2}}{\pi \rho (1-\nu^2)} \right)^{2/5} \simeq 650 \ \ (\mathrm{m/s})^{4/5}, \tag{8}$$

for $E = 74$ GPa, $\rho = 2{,}500$ kg m^{-3}, and $\nu = 0.2$ the Young's modulus, density, and Poisson's ratio of the particles' glass. This implies that 140 kHz $< f_{Hertz} <$ 220 kHz for $0.1 \times \sqrt{gd} < \delta V < \sqrt{gd}$, with $\sqrt{gd} = 0.14$ m s^{-1}. While we will not discuss the validity of Bachelet (2018)'s theoretical prediction, and Farin et al. (2018) found the mean frequency of an impact on a rough bed to be between about 1/2 and 2/3 of the mean frequency of an impact on

a smooth bed, this indicates that collisions between particles will generate signals at frequencies right up to the upper limit of our measurements.

In contrast, the coherent vertical oscillations of the particles, due to the motion of each layer over the one below (see Section 3.1.3, Figure 3), can be expected to cause signal modulation at frequencies f_{osc} that are about 1,000 times smaller, with 33 Hz $< f_{osc} <$ 52 Hz.. These oscillation frequencies are of the order of magnitude of $\delta V/d$, corresponding to a typical rate of collisions.

On the other hand, frequencies around $f_h \simeq$ 3–7 kHz in the signal may originate from the typical period of the acoustic wave front propagation though the flow thickness $h = 3$ cm, if we assume an acoustic wave velocity in granular flows of 100–200 m s^{-1} (see e.g., Hostler, 2004; Hostler & Brennen, 2005; Mouraille & Luding, 2008). Note that the velocity of acoustic signals in granular material varies strongly depending on the confining pressure, packing fraction, material involved, etc. Liu and Nagel (1993) found values varying from about 60 to 280 m s^{-1} depending upon the kind of velocity measured, van den Wildenberg et al. (2013) between 80 m s^{-1} and 150 m s^{-1}, and Bonneau et al. (2008) between 40 m s^{-1} and 80 m s^{-1}.

Observations show that the flow thickness oscillates slightly with time (see Figure A1 in the Appendix), possibly due to compression/dilatation waves in the media or to the complex heterogeneity of the flow (see Section 4.2 and Figure C1 in the Appendix). The typical period of these oscillations is 1 s, possibly generating signals at frequencies $f_{flow} \simeq 1$ Hz.

Movies of velocity fluctuations (Movies S3 and S4 in Supporting Information S1) demonstrate the appearance and disappearance of vortices of velocity fluctuations (cf. Figure C1 in the Appendix). These vortices may be similar to the turbulent vortices that develop in rivers and apply fluctuating forces on the bed roughness, generating seismic signals over a wide frequency range 1–10^5 Hz (Gimbert et al., 2014). Turbulent vortices form close to the flowing-static interface due to the shear stress applied by the flow on the bed. The vortices, once formed, grow through coalescence until they reach the thickness of the flow, then break up into smaller vortices, transferring flow energy toward smaller scales (Kolmogorov, 1941). The highest frequencies generated by the vortices are related to the minimum vortex size, that is, the Kolmogorov microscale, which may not be reachable in a granular flow in which the minimum vortex scale is in theory at least two particle diameters 2d. Therefore, in granular flows, we expect lower frequencies to be generated by vortices than those that can be observed in a liquid flow. The typical size of the observed vortices in our granular flows is about 5-8d $\simeq$ 1–1.6 cm and they travel within the flow at velocities of around 1 m s^{-1}. Therefore, these granular vortices may generate waves at frequencies $f_v \simeq$ 60–100 Hz.

Finally, if we assume a wave velocity in the plate of $v_g \simeq 1{,}000$ m s^{-1}, the resonance of the $L \times l = 10$ cm $\times$ 6.5 cm acoustically isolated plate gives rise to fundamental resonance frequencies $f_{p1} \simeq v_g/l \simeq 15$ kHz and $f_{p2} \simeq v_g/L \simeq 10$ kHz, with higher resonances possible throughout the measured frequency range. Let us now analyze the frequency content of the measured signal and compare it to these expected frequencies.

5.1.2. Comparison With Measured Frequencies

Figure 8 shows that signals are generated throughout the frequency range we are able to measure, consistent with our expectations of interparticle collisions. Even though no clear peaks appear in the high-frequency spectra, there are indications of peaks at frequencies 3 kHz $< f <$ 10 kHz for almost all the flows, which may correspond to waves trapped within the flowing granular layer (with expected frequency range 3 kHz $< f_h <$ 10 kHz). These are highlighted in light green in Figures 8c, 8d, 8f, and 8i. Other peaks appear at frequencies between 10 and 20 kHz, which may be related to the plate's fundamental resonances (at $f_{p1} \simeq$ 10 kHz and $f_{p2} \simeq$ 15 kHz), as illustrated in light pink in Figures 8b, 8d, 8e, 8g, and 8h.

In the low-frequency range, Figure 9 shows clear peaks in signal envelope amplitude between 28 and 50 Hz. These frequencies f_{mod} of the acoustic amplitude modulation are clearly in the range of the frequencies f_{osc} associated with the vertical oscillation of the particles at the surface of the flow (Figure 10c). Indeed, accounting for error, all modulation frequencies f_{mod} are within the 30–60 Hz frequency range of f_{osc}, as highlighted in light gray in Figures 9a and 9i.

The acoustic amplitude modulation frequency increases as a function of the inertial number: f_{mod} is extracted from a Gaussian fit in the range 10–70 Hz of the spectrum (Figure 9) and shown as a function of $\langle I \rangle$ in Figure 10b. In addition, almost all the flows exhibit an increase of spectral amplitude at frequencies between 1 and 3 Hz (see

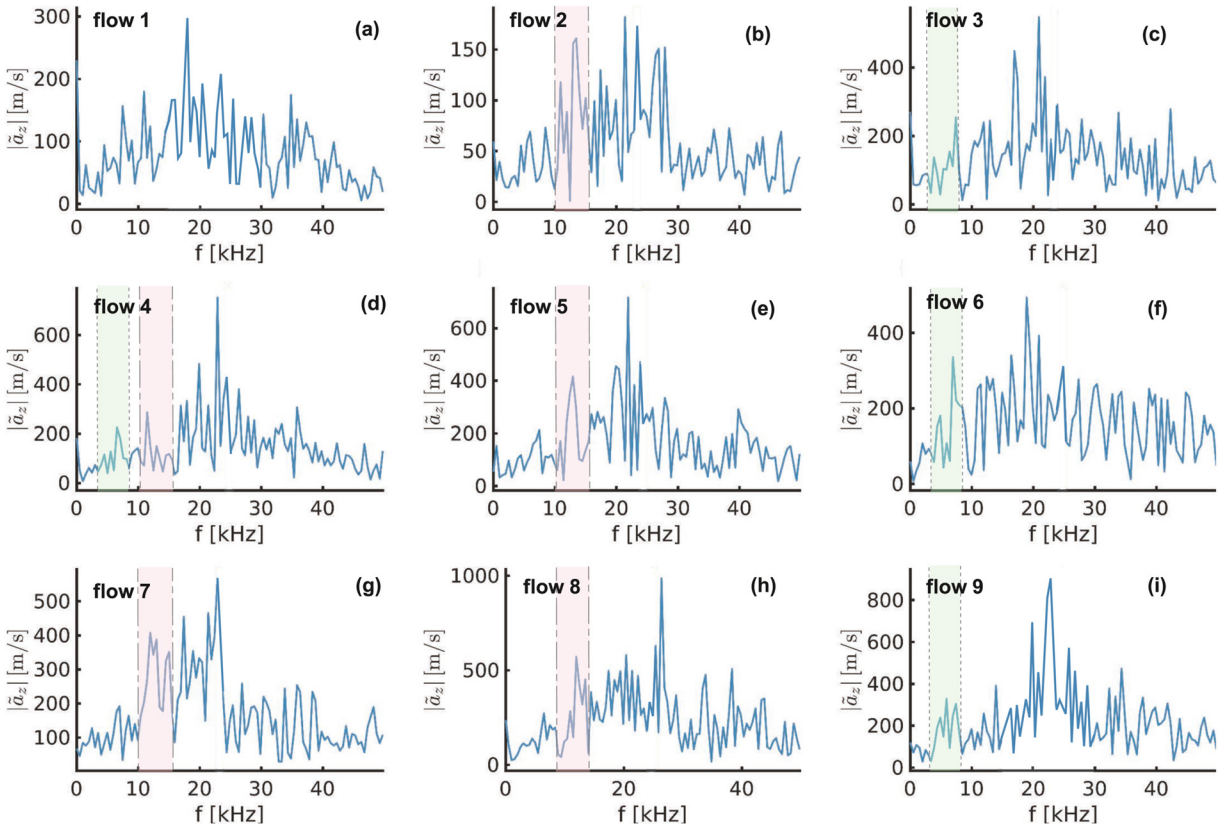

Figure 8. High-frequency ($f > 1$ kHz) spectral amplitude measured for all flows. Letters (a) to (i) refer to flow numbers 1 to 9, corresponding to angles (a–c) $\theta = 16.5°$, (d–f) $\theta = 17.2°$, and (g–i) $\theta = 18.1°$ and to increasing flow thickness along each row (see Table 1 for details). Light pink areas correspond to the frequency range associated with fundamental plate resonances, between f_{p1} and f_{p2}, and light green areas to the frequency range f_h associated with waves trapped in the granular layer.

light pink region in Figure 9). This may correspond to the frequencies of flow oscillations $f_{flow} \simeq 1$ Hz. Some peaks at 15–25 Hz also appear for some flows. Some flows also show a small increase of spectral amplitude at around 60–70 Hz (see Figures 9c and 9f where this frequency range is highlighted in light green) that could be compatible with frequencies $f_v \simeq 60 - 100$ Hz associated with vortices of the velocity fluctuations.

5.2. Acoustic Power

5.2.1. Power Laws and Comparison With Field Observations

We investigate here the relationship between the acoustic power and the properties of the flow, averaged over the granular depth. Figures 11a and 11b show that the acoustic power increases with the depth-averaged velocity fluctuations $\langle \delta V \rangle$ and inertial number $\langle I \rangle$. The range of parameter variation is too low to determine a functional relationship but, conducting a linear regression in log-space, our data are compatible with power law relationships.

$$\Pi_{el} \propto \langle \delta V \rangle^{3.1 \pm 0.9} \propto \langle I \rangle^{2.2 \pm 0.4}. \quad (9)$$

In the field, the seismic power can be calculated from the signal measured at seismic stations and then related to the mean flow velocity, deduced by inverting low-frequency seismic data (Allstadt, 2013; Hibert, Ekström, & Stark, 2017). Field experiments, in which single blocks of different masses were released down a gully, have also shown a correlation between the velocity $\mathbf{V}$ of a block before impact and the seismic energy E_s released during impact (Hibert, Malet, et al., 2017). With this data set, we conducted a linear regression of log E_s against log m and either log $\|\mathbf{V}\|$ or log $|V_z|$, where m is the mass of a block and $\mathbf{V}$ its velocity before impact, with vertical component V_z. When considering the modulus of the velocity, we found that the seismic energy scales as $E_s \propto \|\mathbf{V}\|^{2.4 \pm 0.5}$ (Figure 12a). When considering only the modulus of vertical component of the velocity before impact V_z, the seismic energy scales as $E_s \propto |V_z|^{3.3 \pm 0.8}$ (Figure 12b). Note that the precision on these best fit exponents is

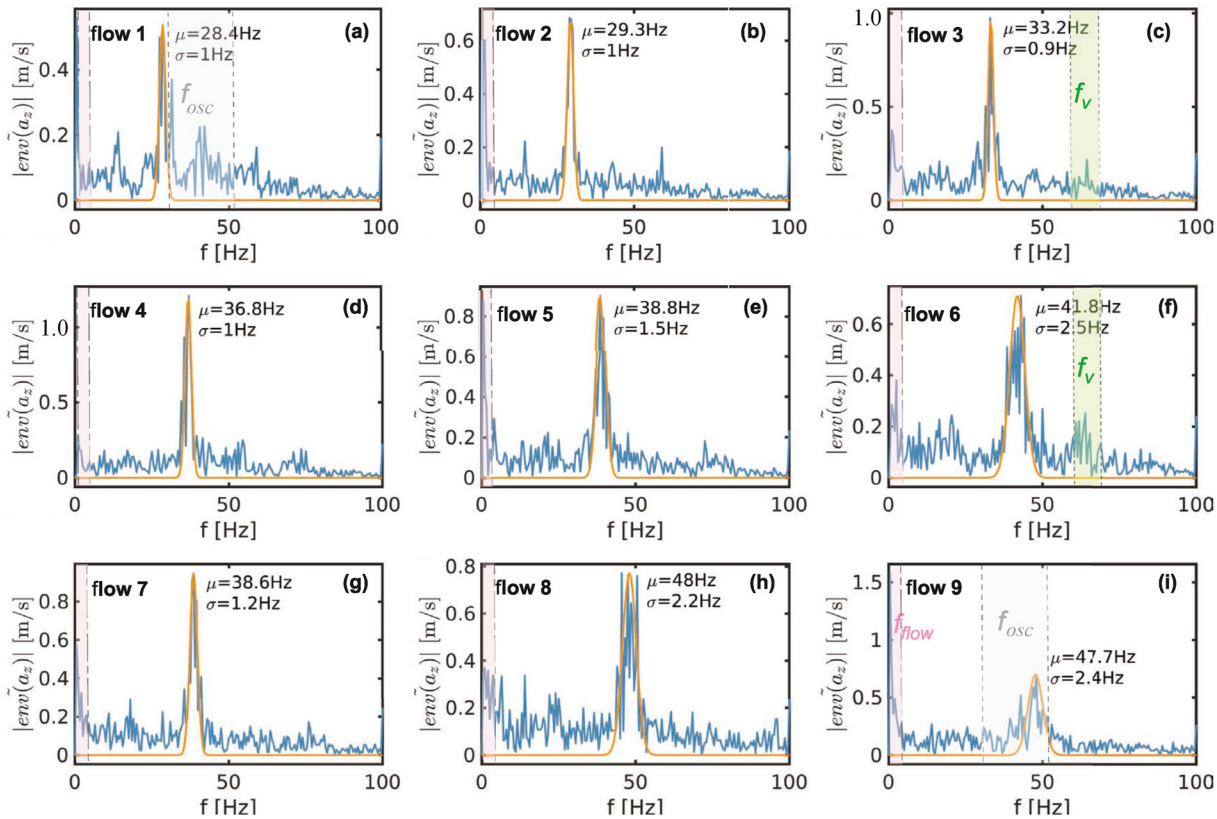

Figure 9. Low-frequency ($f < 100$ Hz) spectral amplitude measured for all flows. Letters (a) to (i) refer to flow numbers 1 to 9, corresponding to angles (a–c) $\theta = 16.5°$, (d–f) $\theta = 17.2°$, and (g–i) $\theta = 18.1°$ and to increasing flow thickness along each row (see Table 1 for details). The orange curves correspond to the Gaussian fits (see Figure 5e). Light gray areas in Figures (a and i) correspond to the frequency range associated with particle oscillations f_{osc}, light pink zones on all the figures correspond to the frequency range of flow oscillations f_{flow} and light green zones to frequency range of vortices f_v. The dashed and dot-dashed vertical lines indicate the boundaries of these zones.

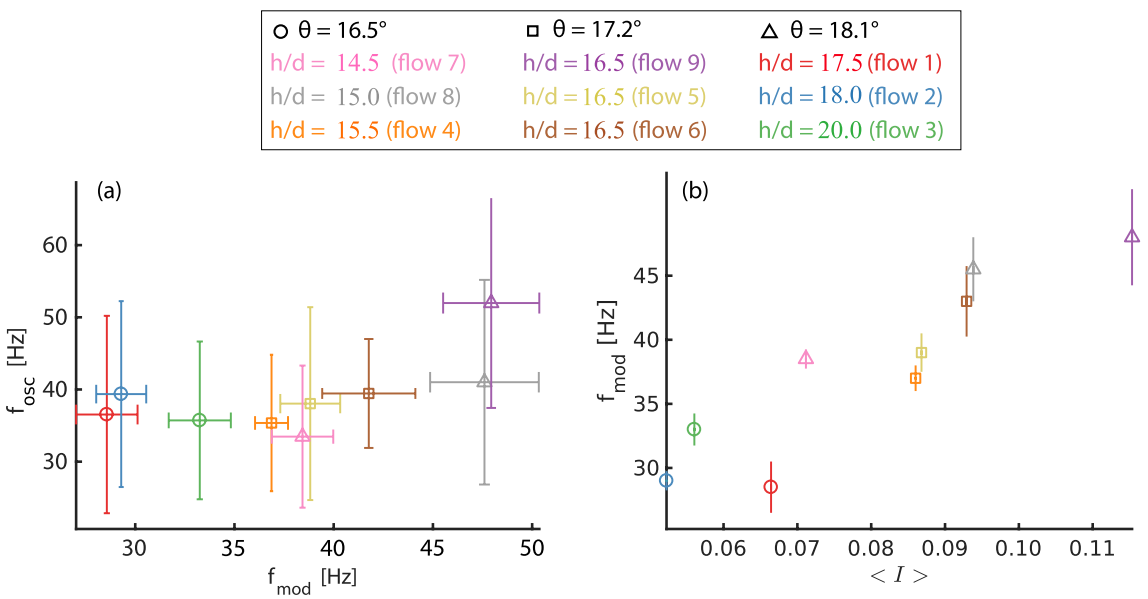

Figure 10. (a) Particles' vertical oscillation frequency f_{osc}, as a function of the frequency f_{mod} of the acoustic amplitude modulation. (b) Acoustic modulation frequency f_{mod} as a function of the average inertial number $\langle I \rangle$.

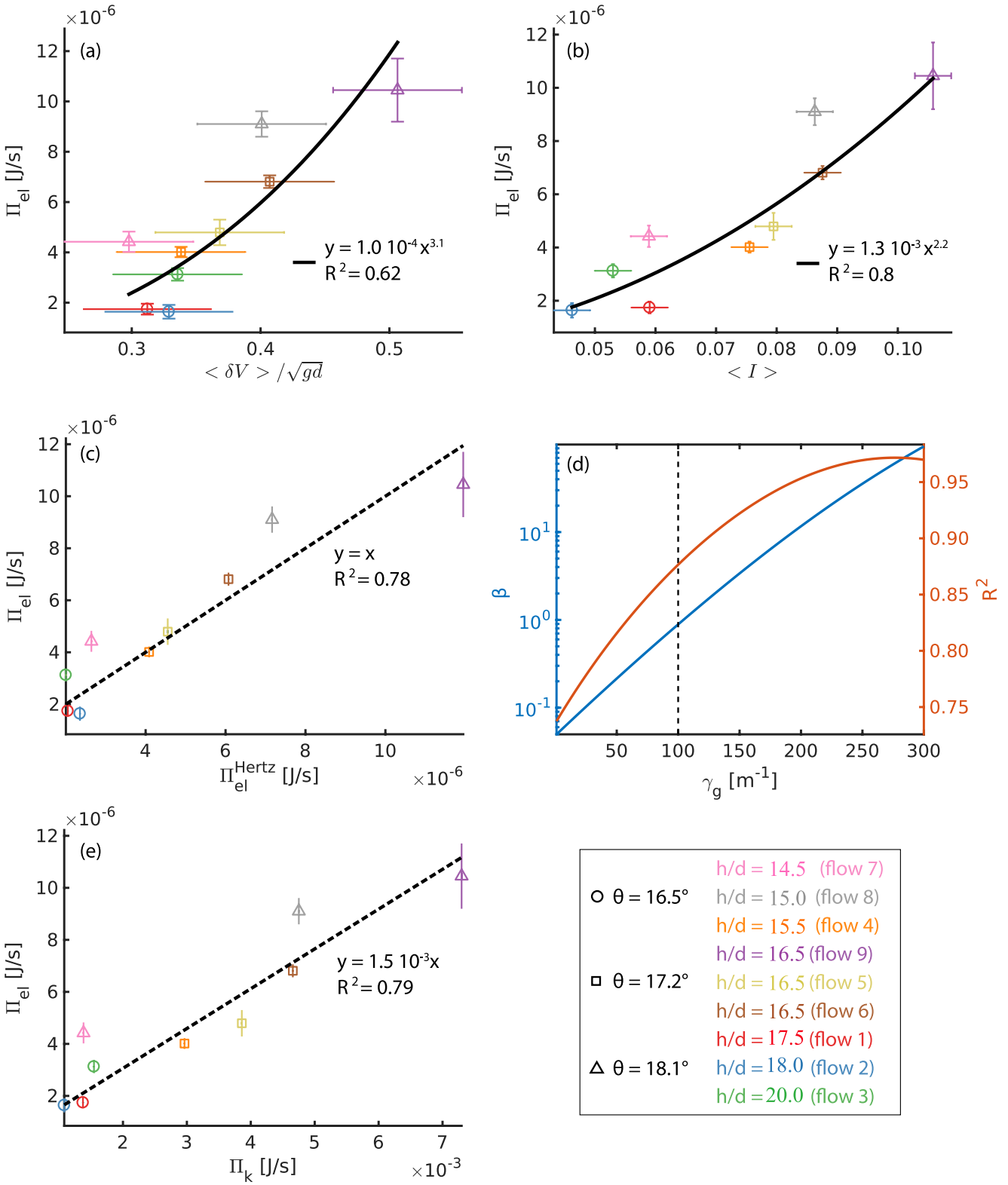

Figure 11. Radiated elastic power Π_{el} as a function of (a) normalized average velocity fluctuations $\langle \delta V \rangle / \sqrt{gd}$ (with $\sqrt{gd} \simeq 0.14$ m/s) and (b) average inertial number $\langle I \rangle$. (c) Experimental Π_{el} versus analytical elastic power Π_{el}^{Hertz} for granular attenuation $\gamma_g = 100$ m^{-1}. (d) Slope β of the best single-regressor linear fit between values $\Pi_{el}^{Hertz}(\gamma_g)$ and Π_{el}, and the associated sum of squared residuals R^2, as a function of the attenuation coefficient γ_g. The vertical black dashed line highlights the case of $\gamma_g = 100$ m^{-1}, the value for which the model gives about the same result as the measurements, that is, $\Pi_{el}^{Hertz}/\Pi_{el} \simeq 1$. (e) Comparison between the measured radiated elastic power Π_{el} and available kinetic power Π_k.

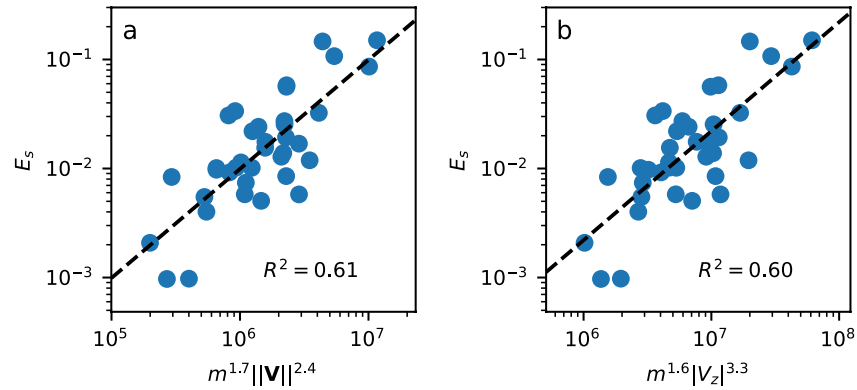

Figure 12. (a) Energy E_s of the seismic signal generated at each individual block impact, as a function of $m^{\alpha}\|\mathbf{V}\|^{\beta}$, for block mass m and modulus of the velocity before impact $\|\mathbf{V}\|$, with the exponents α and β inferred to get the best fit by linear regression and (b) as (a), except with $|V_z|$ rather than $\|\mathbf{V}\|$. All quantities are in SI units and rockfall data are from Hibert, Malet, et al. (2017).

low, since the fit quality of this form is moderate, with R^2 between 0.6 and 0.7, and that they were obtained for single blocks and not for granular flows. Nevertheless, the dependence of E_s on impact velocity may be compared to the dependence of Π_{el} on $\langle \delta V \rangle$ in our laboratory measurements, in Equation 9. Note that similar scaling laws linking seismic wave characteristics to dynamic properties have been found for granular flows and for natural single-block rockfalls (e.g., (Hibert, Ekström, & Stark, 2017; Hibert, Malet, et al., 2017; Schneider et al., 2010)).

5.2.2. Simple Model for Acoustic Emission

Based on the understanding of the seismic source gained above, we propose a simple model that makes it possible to recover the radiated elastic power from particles' velocity fluctuations (i.e., the square root of the granular temperature). We assume that (a) the elastic waves are generated during binary collisions between particles in adjacent layers, at speeds corresponding to the particles' fluctuation velocities, (b) collisions are described by the Hertz contact law and the radiated elastic energy is the work done by the impact force during the contact (Farin et al., 2015; Johnson, 1987), and (c) the acoustic waves propagate from the layer where they are generated down to the bottom of the channel. Attenuation in granular media is frequency dependent (Leclercq et al., 2017; Legland et al., 2012; Martin et al., 2018) and evolves with the reconfiguration of force chains during the flow (as illustrated by Lherminier et al. (2014)), but for the sake of simplicity we assume here that attenuation with distance to the bottom is frequency independent, with constant attenuation coefficient γ_g.

Attenuation in granular media varies strongly, depending on the confining pressure, packing fraction, signal frequency, etc. Different values are reported in the literature, varying between 15 m^{-1} and 150 m^{-1}: for example, Voronina and Horoshenkov (2004) and Chrzaszcz (2016) found $\gamma_g = 100$ m^{-1} and Hostler and Brennen (2005) found values between 25 m^{-1} and 50 m^{-1}.

In our model, the total elastic power is obtained by summing up the contributions of all layers:

$$\Pi_{el}^{Hertz} = \sum_{i=1}^{n} N_i \, W_{el,Hertz}^{i} \, e^{-\gamma_g y_i}, \tag{10}$$

where $W_{el,Hertz}^{i}$ is the typical elastic energy radiated during the impact of a particle in layer i, y_i is the height of the center of the layer i, $e^{-\gamma_g y_i}$is the exponential decay of the wave energy with distance to the bottom, N_i is the rate of impacts in layer i, and n is the number of layers.

The elastic energy radiated during an impact is computed from Hertz contact theory (Farin et al., 2015), under the assumption that the force between two particles is transmitted, attenuated but undistorted, to a thin plate with a frequency-independent velocity response to forcing. Then,

$$W_{el,Hertz}^{i} = a_0 \left(\frac{d}{2}\right)^5 (\delta V(y_i))^{11/5}, \tag{11}$$

with $\delta V(y_i)$ the velocity fluctuation in layer i and a_0 a prefactor involving the elastic parameters of the particles and the PMMA plate (Bachelet et al., 2018). For bending modulus, density, and thickness of the plate

$B = 425$ kg m^2 s^{-2}, $\rho_p = 1{,}180$ kg m^{-3}, and $h_p = 0.01$ m, and Young's modulus, Poisson's ratio, and density of the glass particles $E = 74$ GPa, $\nu = 0.4$, and $\rho = 2{,}500$ kg m^{-3},

$$a_0 \simeq 2.1 \frac{1}{\sqrt{B\rho_p h_p}} \left(\frac{E}{2\left(1-\nu^2\right)} \rho^4 \right)^{2/5} \simeq 1.4 \times 10^8 \,\mathrm{kg\,m^{-5}} \left(\mathrm{m\,s^{-1}}\right)^{-1/5}. \tag{12}$$

The rate of impacts in layer i is given by the following equation:

$$N_i = \frac{\phi l L}{\pi \left(\frac{d}{2}\right)^2} f_i, \tag{13}$$

with the ratio of areas corresponding to the number of particles above the monitored plate of size $L \times l$, and f_i equal to the number of impacts per particle and per unit time. Impacts are assumed to occur when a particle overrides another particle of the layer below at their relative downslope velocity so that

$$f_i = \frac{\langle V_x \rangle(y_i) - \langle V_x \rangle(y_{i-1})}{d} = \dot{\gamma}(y_i). \tag{14}$$

Combining Equations 10, 11, 13, and 14 leads to the final expression of the analytical radiated elastic power:

$$\Pi_{el}^{Hertz} = \frac{a_0 \phi l L}{8\pi} d^3 \sum_i \dot{\gamma}(y_i) \delta V(y_i)^{11/5} e^{-\gamma_g y_i}. \tag{15}$$

Using Equation 15, the acoustic power is expected to scale as follows:

$$\Pi_{el} \propto \langle \delta V \rangle^{16/5}. \tag{16}$$

Because our optical observations showed that $\delta V \propto (\dot{\gamma} d) \propto I^{0.5}$, Π_{el} is also predicted to be proportional to $\langle \dot{\gamma} \rangle^{3.2}$ or $\langle I \rangle^{1.6}$. Despite our inability to measure all power imparted to the plate, due to the limited frequency range of our accelerometers, this is in very good agreement with the scaling observed in Figure 11a, which suggests $\Pi_{el} \propto \langle \delta V \rangle^{3.1 \pm 0.9}$, and in reasonable agreement with the scaling observed in Figure 11b, which suggests $\Pi_{el} \propto \langle I \rangle^{2.2 \pm 0.4}$. Nonetheless, as previously noted, the narrow range of our experiments makes it very difficult to discriminate between different power-law exponents or functional relationships.

To compare our observations with those of Taylor and Brodsky (2017), we have to note that the value E_a that they called "acoustic energy" is a term proportional to the square of the acceleration, rather than the square of velocity. As a consequence of this and of Equation 7, which indicates that typical signal accelerations are a factor $a_0' d^{-1} \delta V^{1/5}$ larger than typical signal velocities, we expect that $E_a \propto \langle \delta V \rangle^{2/5} \Pi_{el}$. This would imply that, according to our theory, $E_a \propto \langle \delta V \rangle^{18/5} = \langle \delta V \rangle^{3.6}$ or, if we assume the power laws $\delta V \propto I^{0.5}$ and $\Pi_{el} \propto \langle I \rangle^{2.2 \pm 0.4}$ of Equations 6 and 9, that $E_a \propto \langle I \rangle^{2.4 \pm 0.4}$. Taylor and Brodsky (2017)'s observations, however, suggest that $E_a \propto I$. This difference may be due to the fact that their setting is very different from ours, to error in their calculation of I (which they estimate by assuming a shear layer thickness of 5d, for all experiments) or to the limitations of our simple model.

The key parameter in the calculation of Π_{el}^{Hertz} is the attenuation factor. If we take $\gamma_g = 100$ m^{-1}, we obtain a very good agreement with the measured acoustic power (Figure 11c). However, the value of Π_{el}^{Hertz} is very sensitive to γ_g, as shown in Figure 11d. For example, if $\gamma_g = 50$ m^{-1}, $\Pi_{el}^{Hertz} \simeq 0.5 \Pi_{el}$. Figures 13a and 13b show that with $\gamma_g = 100$ m^{-1}, the main contributions to the acoustic power come from the grains near the surface, while with $\gamma_g = 300$ m^{-1}, they come from the grains located in the middle of the granular layer, where velocities and velocity fluctuations are small. Bachelet et al. (2018)'s measurements of acoustic energy transmission through static grain packs suggest an attenuation constant $\gamma_g = 220$ m^{-1} for our $d = 2$ mm grains, but such transmission is affected by the structure of the grain pack (Lherminier et al., 2014), which may be significantly different in granular flows. Precise attenuation measurements will be a crucial step to further validate our simple model and will be performed in the future.

Another key issue is the difference between the fluctuations measured near the side walls and those within the flow, as observed in the discrete element simulations of Hanes and Walton (2000) and discussed in Section 4.2. To assess how the predicted acoustic power would change if measurements were performed in the flow's center,

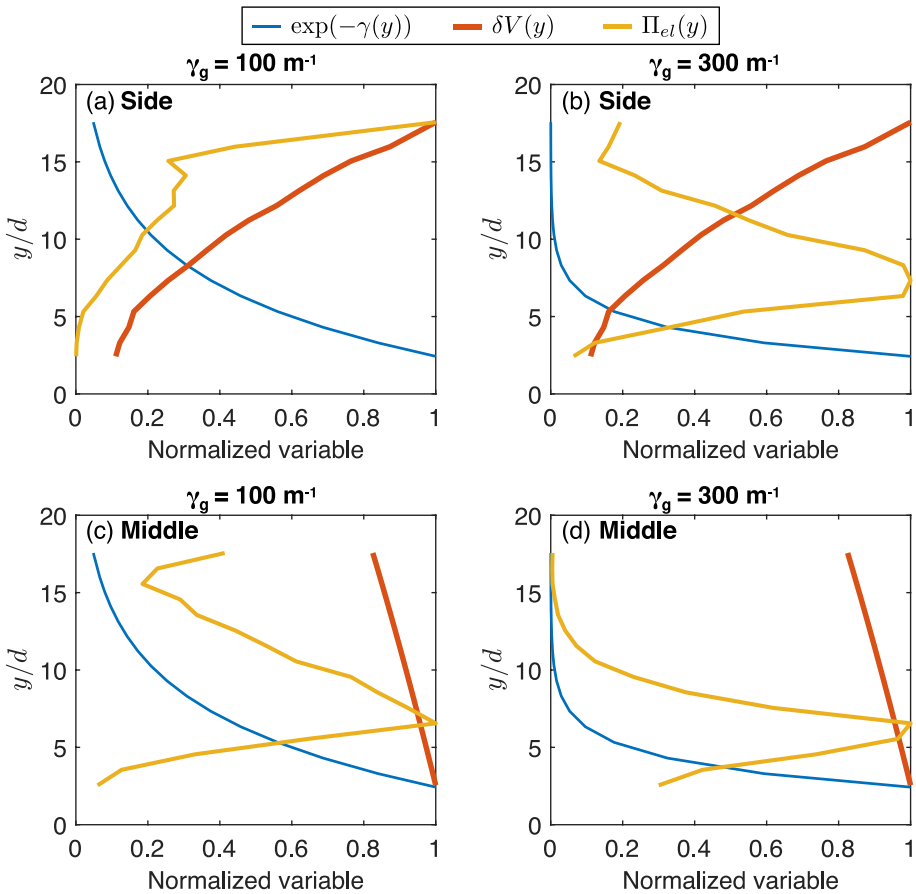

Figure 13. (a, b) Normalized contributions $N_i W^i_{el,Hertz} e^{-\gamma_g y_i}$ to analytical acoustic power Π_{el}, as a function of depth y_i/d and computed using the fluctuating speed δV measured along the side of the flow in experiment 1, for (a) $\gamma_g = 100$ m^{-1} and (b) $\gamma_g = 300$ m^{-1}. (c and d) Equivalent normalized contributions, assuming a linear granular temperature profile increasing with depth, as might be observed in the middle of the flow, for (c) $\gamma_g = 100$ m^{-1} and (d) $\gamma_g = 300$ m^{-1}. In each panel, attenuation $\exp(-\gamma_g y)$ is also represented.

we calculate Π^{Hertz}_{el} for profiles of the fluctuating velocity that mimic those in the simulations of Hanes and Walton (2000) (their Figure 15). Specifically, we take the same value δV_s of the fluctuating velocity δV as at the free surface but suppose that δV, instead of decreasing down to the bottom, increases linearly to reach $\delta V(d) = 1.2\delta V_s$. This assumption corresponds to the following equation:

$$\Pi^{Hertz}_{el} = \sum_i \frac{\phi l L}{\pi (d/2)^2} f_i a_0 (d/2)^5 (1.2\delta V_s (1 - y_i/h) + \delta V_s y_i/h)^{11/5} e^{-\gamma_g y_i}. \quad (17)$$

Assuming that the collision frequency is $f_i = \delta V_i/d = (1.2\delta V_s(1 - y_i/h) + \delta V_s y_i/h)/d$ further leads to

$$\Pi^{Hertz}_{el} = \frac{a_0 \phi l L h d}{8\pi} \delta V_s^{16/5} \int_0^1 (1.2 - 0.2z)^{16/5} e^{-\gamma_g h z} dz. \quad (18)$$

Note that when we make this assumption on the $\delta V(y)$ profile, the main contribution to the acoustic power comes from slightly below the middle of the granular layer, regardless of whether the attenuation coefficient is $\gamma_g = 100$ m^{-1} or $\gamma_g = 300$ m^{-1} (Figures 13c and 13d).

5.2.3. Acoustic Versus Kinetic Energy

Finally, we construct a model linking acoustic emissions to the mean kinetic energies of grains in each flow layer,

$$E^i_k = \frac{\pi \rho d^3}{12} \left(\|\langle \mathbf{V} \rangle\| (y_i)^2 + \delta V (y_i)^2 \right), \quad (19)$$

by adding to our previous model the somewhat arbitrary assumption that the conversion coefficient from kinetic to attenuation-adjusted acoustic energy, that is, the energy ratio or acoustic efficiency $W^i_{el,Hertz}/E^i_k$, is constant for each impact and equal to ξ. We then replace the term $W^i_{el,Hertz}$ in Equation 10 by $\xi\, E^i_k$ to recover the prediction $\Pi_{el} = \xi\Pi_k$, for available kinetic power

$$\Pi_k = \sum_i N_i\, E^i_k\, e^{-\gamma_g y_i}. \tag{20}$$

Figure 11e shows that, over our experiments, the measured acoustic power is approximately proportional to Π_k and the implied energy ratio is $\xi = 1.5 \times 10^{-3}$.

In contrast, the experiments of Bachelet et al. (2018) measured a mean energy conversion coefficient, after adjustment for attenuation, of $\xi \simeq 0.13$. Basal properties in those experiments were identical to this study's but grains had greater mean density ρ, Young's modulus E, diameter d, and velocity $\mathbf{V}$. Furthermore, each impact was between a falling grain and a static, horizontal base, so that, generalizing δV to be the normal impact velocity, $\delta V \simeq \|\mathbf{V}\|$. In our case, meanwhile, $\Pi^{Hertz}_{el} \simeq \Pi_{el}$ and Π_k are dominated by contributions from near-surface impacts, for which Figure 7d indicates that $\delta V \simeq 0.28\|\mathbf{V}\|$. Since, generalizing the definitions of $W^i_{el,Hertz}$, E^i_k, $\|\langle \mathbf{V}^2 \rangle\|$ and Hertz prefactor $a_0 \propto \left(E\rho^4\right)^{2/5}$ to apply to both cases,

$$W^i_{el,Hertz}/E^i_k = \frac{3a_0 d^2}{8\pi\rho} \frac{\delta V^2}{\|\langle \mathbf{V}^2 \rangle\|} \delta V^{1/5}, \tag{21}$$

these differences explain Bachelet et al. (2018)'s measurement of a much larger ξ. Equation 21 also suggests that Π_{el}/Π_k is approximately constant over our experiments only because $\Pi_{el} \simeq \Pi^{Hertz}_{el}$, the base and grains are kept constant, and the nature of our flows does not vary significantly.

However, the energy ratio of 1.5×10^{-3} is comparable to that observed in the field for rockfalls, despite acoustic energy emission depending strongly on the highly variable bed response. As an example, values of $\xi \simeq 10^{-5}$–10^{-3} were found for rockfalls on La Réunion Island (Hibert et al., 2011), on Montserrat Island (Levy et al., 2015), and in the French Alps (Deparis et al., 2008).

6. Conclusion

As seismic waves generated by landslides are continuously recorded by seismic networks, detailed analysis of these signals provides a new way to collect data on the dynamics and rheology of natural flows. This is, however, only possible if quantitative relationships between the flow properties and the acoustic signal characteristics are established.

In the experiments reported here, we provide new quantitative insights into the origin of the acoustic signals generated by dense, almost steady, and uniform granular flows in which persistent contact networks link nearly static basal grains to energetic grains near the surface. By capturing and analyzing high-speed camera footage, we measured the base-normal profiles of mean flow velocity and of root mean square velocity fluctuations, at the flows' lateral boundary, and demonstrated relationships between the fluctuations, the mean velocity, the local shear rate, and the local inertial number. Meanwhile, by capturing and processing accelerometer data, we could associate the flows' acoustic signals with observed flow properties and other physical phenomena: interparticle collisions, fundamental resonances of the flow's base, acoustic standing waves within the flow, vortices of velocity fluctuations, coherent shear and macroscopic flow variations. Then, using the approach of Farin et al. (2016), we estimated the rate of acoustic energy transmission from each flow to its base and empirically related this power to our measurements of both the depth-averaged root mean square velocity fluctuations within the flow and the depth-averaged inertial number, finding the former relation to be consistent with an analytical model in which internal shear leads to Hertzian collisions throughout the flow, the normal forces of which are transmitted, attenuated but undistorted, to a thin elastic plate.

More precisely, our results are consistent with a rate of seismic energy emission, from each region of a granular flow, proportional to the 8/5th power of its granular temperature (the mean squared value of velocity fluctuations). Beyond the interpretation of the generated acoustic signal in terms of granular flow properties, this suggests a method for measuring velocity fluctuations within granular flows, which may help improve our understanding

of the behavior of natural flows near boundaries. Indeed, Artoni & Richard (2015a) suggested that velocity fluctuations (a) are a key ingredient to be included in models describing dense granular flows in the vicinity of an interface and (b) appear in scaling laws reproducing the effective friction at lateral walls. More specifically, force fluctuations related to velocity fluctuations may trigger slip events even if the system is globally below the slip threshold (Artoni & Richard, 2015a). Furthermore, granular temperature is a key parameter of kinetic theories. Its measurement in dense granular flows will help constrain attempts to extend this theory to dense granular flows (Berzi, 2014).

Finally, we consider a distinct acoustic signal, identified at frequencies around a thousand times lower than the maximum measured signal frequency. This signal is shown to correspond to the displacement of particles over one another, related to the coherent relative motion of the grain layers. This seems to result from the quasi monodisperity of the particles involved in these experiments and can be compared to signals identified in the investigation of "booming dunes."

Further studies should investigate the effects of particle size and shape on the generated acoustic signals and extend the range of bed slopes (i.e., velocities), so as to be able to both better discriminate scaling laws between the characteristics of the flow and those of the acoustic signal, and to examine the range of validity of such scaling laws.

Appendix A: Heights of the Flows

The flow height is measured by detecting the boundaries of particles at the free surface of the flow, in each frame captured by the high-speed camera (Figure A1a). Then, the spatial and temporal height profile obtained by repeating the procedure for all instants (Figure A1b) is averaged over time (Figure A1c) and space (Figure A1d).

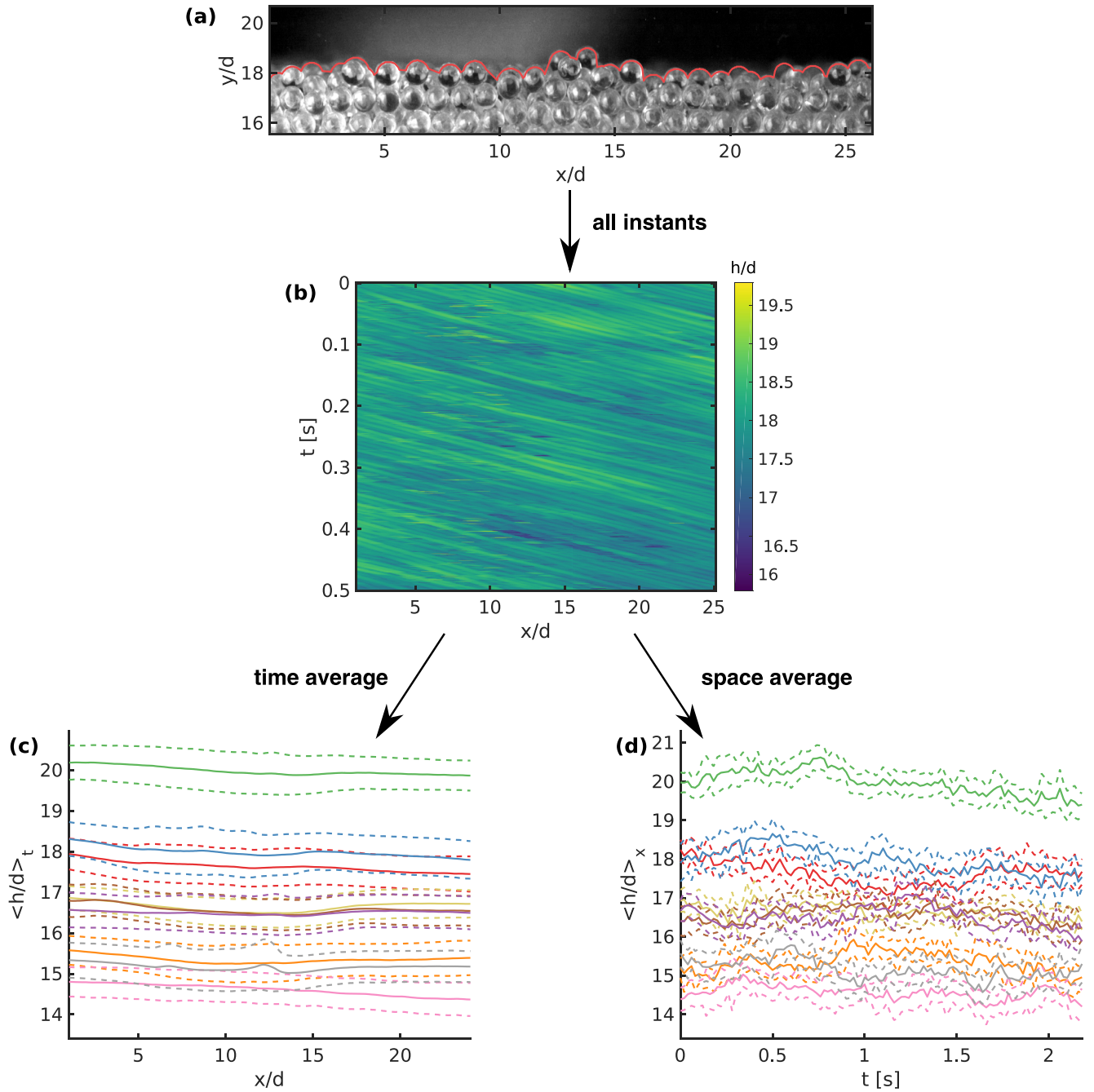

Figure A1. Heights of the flows: (a) example of flow interface detection (red line), (b) space and time height, thereafter averaged over (c) time or (d) space. Each color of panels (c and d) corresponds to a specific flow (see e.g., Figure 11 for detailed legend), while continuous lines correspond to mean values and dashed lines to one standard deviation either side of these means.

Appendix B: Velocity Fluctuation Measurements: Window Effect

The estimate of total velocity fluctuations depends on the width w of the window considered:

$$\delta V^2(y,t) = \frac{1}{w}\int_{y-w/2}^{y+w/2} \left(\mathbf{V}(y',t) - \langle \mathbf{V}\rangle(y,t)\right)^2 dy', \tag{B1}$$

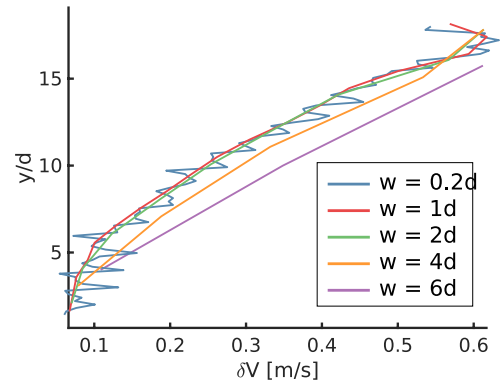

Figure B1. Effect of the window size on the fluctuation velocity computation.

where $\langle \mathbf{V} \rangle(y,t)$ is the average velocity in the center of the box. Since the average vertical velocity equals zero, a first order expansion is $\langle \mathbf{V} \rangle(y,t) = \langle \mathbf{V} \rangle(y',t) - \dot{\gamma}(y)(y'-y)\mathbf{e_x}$, giving the following equation:

$$\delta V^2(y,t) = \frac{1}{w}\int_{y-w/2}^{y+w/2} \left(\delta \mathbf{V}^*(y') + \dot{\gamma}(y)(y'-y)\mathbf{e_x}\right)^2 dy', \tag{B2}$$

with $\delta \mathbf{V}^*(y') = \mathbf{V}(y',t) - \langle \mathbf{V} \rangle(y',t)$. Expanding the square leads to three terms I_1, I_2, and I_3:

$$I_1 = \delta V^{*2}(y,t) = \frac{1}{w}\int_{y-w/2}^{y+w/2} \delta \mathbf{V}^{*2}(y')dy', \tag{B3}$$

$$I_2 = \frac{2}{w}\int_{y-w/2}^{y+w/2} \dot{\gamma}(y)(y'-y)\delta V_x(y')dy', \tag{B4}$$

$$I_3 = \frac{1}{w}\int_{y-w/2}^{y+w/2} \left(\dot{\gamma}(y)(y'-y)\right)^2 dy' = \frac{w^2\,\dot{\gamma}^2(y)}{12}. \tag{B5}$$

I_1 corresponds to the genuine mean of velocity fluctuations at each point. I_2 can be computed by a first order expansion of $\delta V_x(y')$:

$$\delta V_x(y') = \delta V_x(y) + \frac{d\delta V_x}{dy}(y)(y'-y). \tag{B6}$$

Thus,

$$I_2 = \frac{2}{w}\left(\delta V_x(y)\int_{y-w/2}^{y+w/2}(y'-y)dy' + \frac{d\delta V_x}{dy}(y)\int_{y-w/2}^{y+w/2}(y'-y)^2 dy'\right). \tag{B7}$$

The first term equals zero, whereas the second can be neglected because of the second order.

Finally, total velocity fluctuations estimate are given by the following expression:

$$\delta V^2(y,t) = \delta V^{*2}(y,t) + \frac{w^2\,\dot{\gamma}^2(y)}{12}. \tag{B8}$$

The second term quantifies the error introduced by considering the average velocity taken in y (the center of the box) instead of the value in y' in Equation B1. Its expression is very similar to the one found by Weinhart et al. (2013) (Equation 34). The only difference comes from the choice of the averaging function, also called the coarse-graining function. We implicitly chose a gate equal to one in $[y - w/2, y + w/2]$ and to zero elsewhere, whereas a more complex choice is usually selected for differentiability (Glasser & Goldhirsch, 2001; Weinhart et al., 2013).

Thanks to Equation B8 and approximating δV^* by 2.1 $d\,\dot{\gamma}$, as suggested by the linear fit in Figure 7e, it is possible to deduce that the windows have an effect similar to that of δV^* when w = 5d. For this reason, the window is negligible in our case (see Figure B1).

Appendix C: Correlation Lengths Within the Flow

To obtain quantitative measurements of the correlation length of velocity fluctuations we compute the downslope and vertical velocity correlations between two points M_1 and M_2 with coordinates (x_1, y_1) and (x_2, y_2): Figure C1

$$C_{V_i}(M_1, M_2) = \frac{\sum_t \delta V_i(M_1, t) \times \delta V_i(M_2, t)}{\sqrt{\sum_t \delta V_i(M_1, t)^2} \times \sqrt{\sum_t \delta V_i(M_2, t)^2}}, \tag{C1}$$

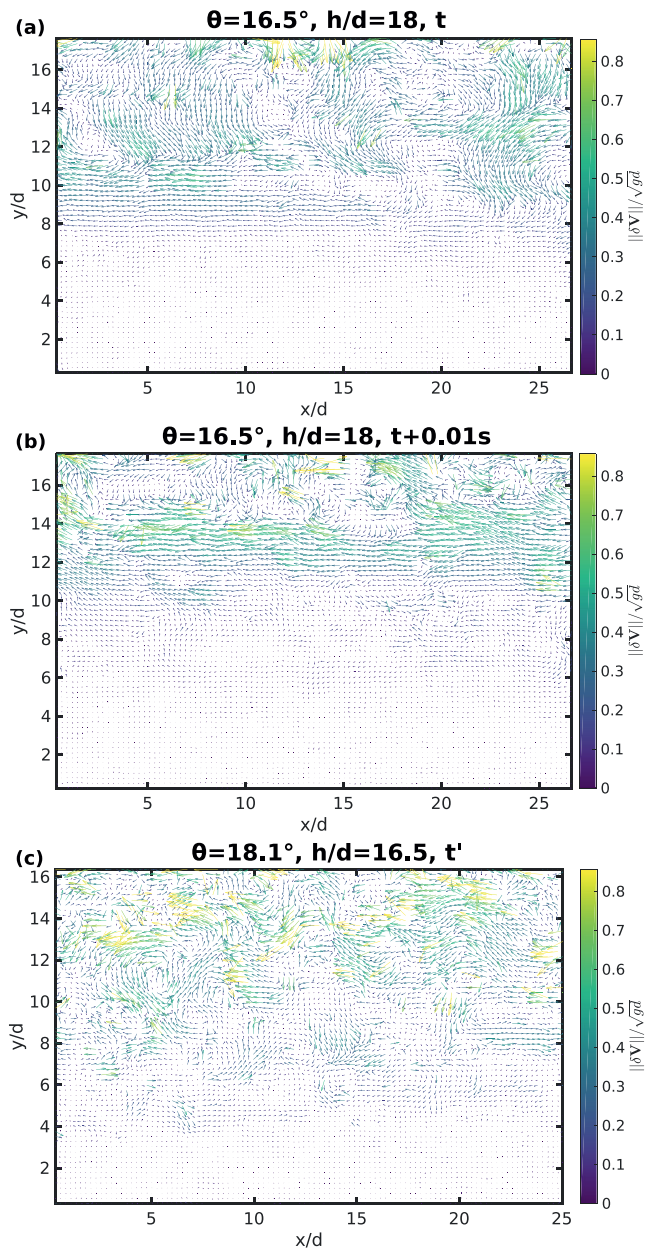

Figure C1. Map of velocity fluctuations obtained with Correlation Image Velocimetry for flow number 2 (a and b) and 9 (c) at instants t, $t + 0.01$ s, and t', respectively (t and t' are arbitrary).

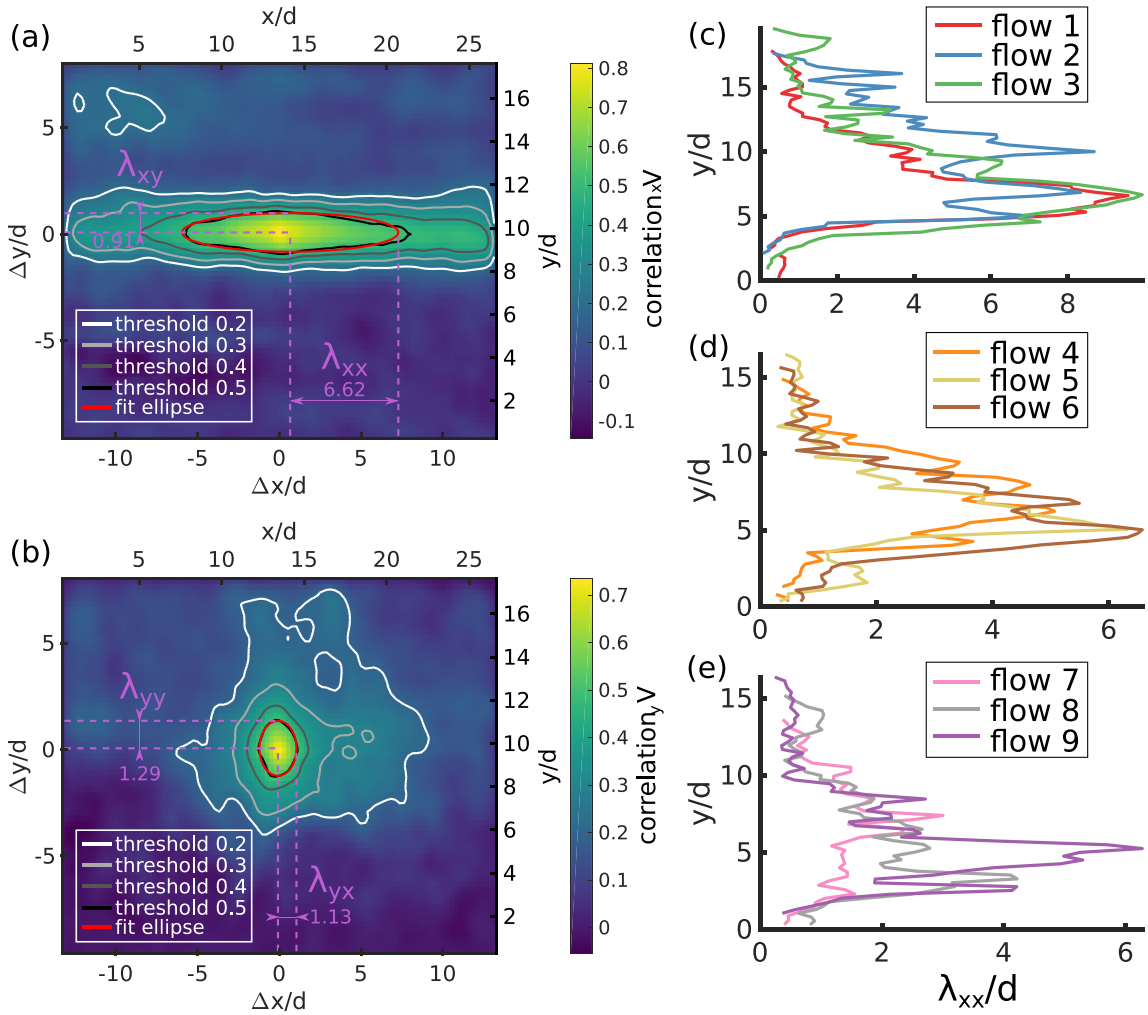

Figure C2. Example of spatial correlations between the (a) downslope and (b) base-normal components of fluctuating grain velocities, between the static point of coordinates ($x/d = 14$, $y/d = 10$) and all the others positions for the flow 2. Panels (c) to (e) correspond to the correlation length λ_{xx} of the horizontal velocity in x direction for all the flows.

where $i = x, y$. Examples of downslope and vertical velocity correlations are presented in Figures C2a and C2b, respectively. High correlations of the horizontal velocity over one particle thickness are clearly visible. To quantify this correlation, a correlation length has been defined. It corresponds to the length at which the correlation reaches a given threshold. Unlike Pouliquen (2004), who chose a threshold of 0.05, we selected a value of 0.5 because of the limitation of the window of observation (see the dark gray contour plot of Figure C2a, which seems cropped by the right border of the window). The correlation length increases with decreasing slope angle as observed by Pouliquen (2004) and Staron (2008) or in granular flows approaching jamming (Gardel et al., 2009). In our experiments, only the lengths of downslope velocities in the x-direction λ_{xx} are higher than one particle diameter. This suggests correlated motion of particles of the same layer, supporting the layering observed in Figure 3b. In agreement with Pouliquen (2004) and Staron (2008), correlation lengths decrease for increasing slope angles (Figures C2c–C2e), as observed in Movies S3 and S4 (Supporting Information S1). The correlation lengths collapse to zero under $y/d = 5$ because particle velocities are smaller than noise.

Note that for dry granular chute flows (Gardel et al., 2009) and for granular flows in a fluid (Orpe & Kudrolli, 2007), significantly greater spatial correlations are observed near the boundaries, which may be the case here.

Notation

a'_0	Hertzian frequency coefficient ((m/s)$^{4/5}$) (see Equation 8)
a_0	Hertzian energy coefficient (kg m^{-5} (m/s)$^{-1/5}$) (see Equation 12)
a_z	vibratory acceleration of the basal plate (m s^{-2})
$\lvert\tilde{a}_z\rvert$	amplitude spectrum of the vibratory acceleration (m s^{-1})
a^*, b^*	coefficients of a best fit polynomial for a mean downslope velocity profile (−)
B	Bending stiffness of the basal plate (J)
d	representative grain diameter (m)
E	young's modulus of the grains' material (Pa)
E_a	"acoustic energy" defined by Taylor & Brodsky (2017)(m^2 s^{-2})
E_k^i	mean kinetic energy of a grain in layer i (J)
E_s	seismic energy generated by a block impact of Hibert, Malet, et al. (2017) (J)
f	frequency of the vibration signal (Hz)
f_i	theoretical number of impacts per particle in layer i, per time unit (s^{-1})
f_{Hertz}	mean signal frequency predicted by Bachelet (2018) (Hz) (see Equation 7)
f_h, f_{p1}, f_{p2}	frequencies associated with trapped waves and fundamental resonances of the basal plate (Hz) (see Section 5.1.1)
f_{flow}, f_v	frequencies associated with macroscopic flow variation and vortices of velocity fluctuations (Hz) (see Section 5.1.1)
f_{osc}	frequency of grain oscillation during coherent shear (Hz)
f_{mod}	frequency of acoustic modulation (Hz)
g	gravitational acceleration (m s^{-2})
h	flow thickness (m)
h_g	gate elevation (m)
h_p	thickness of the basal plate (m)
I, $\langle I\rangle$	local and depth-averaged inertial number (−) (see Equation 4)
L, l	length and width of the acoustically isolated plate (m)
M	mass of the acoustically isolated plate (g)
N_i	number of impacts per unit time in particle layer i (s^{-1})
n	number of particle layers (−)
P	hydrostatic pressure (Pa)
T	granular temperature (m^2 s^{-2})
t	time (s)
$\mathbf{V} = (V_x, V_y)$	grain velocity, downslope and normal to the base (m s^{-1})
$\langle\mathbf{V}\rangle = (\langle V_x\rangle), \langle V_y\rangle)$	average velocities within each layer (m s^{-1})
V_{xs}, $\langle\langle V_x\rangle\rangle$	surficial and depth-averaged mean downslope grain velocity (m s^{-1})
v_g	group velocity of the A_0 mode in PMMA ($\simeq$1,000 m s^{-1})
v_z	normal vibration velocity of the plate (m s^{-1})
w	thickness of the layers over which averages are calculated (m)
W_{el}	radiated elastic energy (J)
$W^i_{el,Hertz}$	theoretical energy radiated from a collision in layer i (J)
x, y	downslope and base-normal positions of the particles (m)
Y	fitting parameter for Josserand et al. (2004)'s mean velocity profiles (m)
$\dot{\gamma}$	shear rate (s^{-1})
γ_g	characteristic attenuation coefficient of acoustic energy in granular media (m^{-1})
γ_p	attenuation coefficient of acoustic energy in the basal plate (m^{-1})
Δt	duration (s)
δV_x^2, δV_y^2	variances of grains' velocity components, within each layer (m^2 s^{-2})
δV, δV_s, $\langle\delta V\rangle$	local, surficial, and depth-averaged RMS fluctuating velocity (m s^{-1})
θ	slope angle (°)
ν	Poisson's ratio of the grains' material (−)
ξ	proportion of kinetic energy converted to acoustic energy in a collision (−)
Π_{el}	radiated elastic power (J s^{-1})
Π_{el}^{Hertz}	analytical radiated elastic power (J s^{-1})

Π_k	available kinetic power (J s^{-1})
ρ, ρ_p	densities of the grains and the basal plate (kg m^{-3})
τ_i, τ	empirical periods of a particle's oscillations and their median (s)
ϕ	volumetric packing fraction (−)
ϕ_{2D}	surface packing fraction at the side wall (−)

Data Availability Statement

The experimental data and scripts used in this article are available at Bachelet et al. (2020).

Acknowledgments
We thank Xiaoping Jia, Sylvain Viroulet, Diego Berzi and Alexandre Valance for insightful discussions on granular temperature and kinetic theory. We thank Göran Ekström for sharing the inverted force history for the Mt Dall, Mt Lituya, Sheemahant Glacier, and Lamplugh Glacier landslides. We thank Alain Steyer for his great help in mounting the setup. This work has been mainly funded by the contract ERC-CG-2013-PE10-617472 SLIDEQUAKE. RT acknowledges the support of the INSU ALEAS and the France-Norway IRP D-FFRACT programs, and of the Research Council of Norway through its Centres of Excellence funding scheme, Project No. 262644. MIA acknowledges the support of the Georgetown Environmental Justice Program.

References

Akay, A. (2002). Acoustics of friction. *Journal of the Acoustical Society of America*, *111*(4), 1525–1548. https://doi.org/10.1121/1.1456514

Aleshin, V., Gusev, V., & Tournat, V. (2007). Acoustic modes propagating along the free surface of granular media. *Journal of the Acoustical Society of America*, *121*(5), 2600–2611. https://doi.org/10.1121/1.2714923

Allstadt, K. (2013). Extracting source characteristics and dynamics of the august 2010 mount meager landslide from broadband seismograms. *Journal of Geophysical Research: Earth Surface*, *118*(3), 1472–1490. https://doi.org/10.1002/jgrf.20110

Allstadt, K., Matoza, R., Lockhart, A., Moran, S., Caplan-Auerbach, J., Haney, M., et al. (2018). Seismic and acoustic signatures of surficial mass movements at volcanoes. *Journal of Volcanology and Geothermal Research*, *364*, 76–106. https://doi.org/10.1016/j.jvolgeores.2018.09.007

Allstadt, K. E., Farin, M., Iverson, R. M., Obryk, M. K., Kean, J. W., Tsai, V. C., et al. (2020). Measuring basal force fluctuations of debris flows using seismic recordings and empirical green's functions. *Journal of Geophysical Research: Earth Surface*, *125*(9), e2020JF005590. https://doi.org/10.1029/2020JF005590

Ancey, C. (2001). Dry granular flows down an inclined channel: Experimental investigations on the frictional-collisional regime. *Physical Review*, *65*(1), 011304. https://doi.org/10.1103/PhysRevE.65.011304

Andreotti, B. (2004). The song of dunes as a wave-particle mode locking. *Physical Review Letters*, *93*(23), 238001. https://doi.org/10.1103/PhysRevLett.93.238001

Andreotti, B. (2012). Sonic sands. *Reports on Progress in Physics*, *75*(2), 026602. https://doi.org/10.1088/0034-4885/75/2/026602

Andreotti, B., Forterre, Y., & Pouliquen, O. (2013). Granular media between fluid and solid. https://doi.org/10.1017/CBO9781139541008

Arran, M., Mangeney, A., de Rosny, J., Farin, M., Toussaint, R., & Roche, O. (2021). Laboratory landquakes: Insights from experiments into the high-frequency seismic signal generated by geophysical granular flows. *Journal of Geophysical Research: Earth Surface*, *126*(5), e2021JF00617. https://doi.org/10.1029/2021JF006172

Artoni, R., & Richard, P. (2015a). Effective wall friction in wall-bounded 3D dense granular flows. *Physical Review Letters*, *115*(15), 158001. https://doi.org/10.1103/physrevlett.115.158001

Artoni, R., & Richard, P. (2015b). Average balance equations, scale dependence, and energy cascade for granular materials. *Physical Review*, *91*(3), 032202. https://doi.org/10.1103/physreve.91.032202

Bachelet, V. (2018). *Étude expérimentale des émissions acoustiques générées par les écoulements granulaires (Unpublished doctoral dissertation)*. Institut de Physique du Globe de Paris.

Bachelet, V., Mangeney, A., de Rosny, J., Toussaint, R., & Farin, M. (2018). Elastic wave generated by granular impact on rough and erodible surfaces. *Journal of Applied Physics*, *123*(4), 044901. https://doi.org/10.1063/1.5012979

Bachelet, V., Mangeney, A., de Rosny, J., Toussaint, R., Farin, M. , & Hibert, C. (2020). Stationary granular flow seismicity and optics. *Zenodo*. https://doi.org/10.5281/zenodo.3600306

Berzi, D. (2014). Extended kinetic theory applied to dense, granular, simple shear flows. *Acta Mechanica*, *225*(8), 2191–2198. https://doi.org/10.1007/s00707-014-1125-1

Berzi, D., & Jenkins, J. T. (2011). Surface flows of inelastic spheres. *Physics of Fluids*, *23*(1), 013303. https://doi.org/10.1063/1.3532838

Bonneau, L., Andreotti, B., & Clément, E. (2008). Evidence of Rayleigh-hertz surface waves and shear stiffness anomaly in granular media. *Physical Review Letters*, *101*(11), 118001. https://doi.org/10.1103/physrevlett.101.118001

Calder, E. S., Cortés, J. A., Palma, J. L., & Luckett, R. (2005). Probabilistic analysis of rockfall frequencies during an andesite lava dome eruption: The soufrière hills volcano, Montserrat. *Geophysical Research Letters*, *32*(16), L16309. https://doi.org/10.1029/2005GL023594

Chrzaszcz, K. (2016). Ondes dans les milieux granulaires: de l'échelle microscopique à l'échelle macroscopique. (Unpublished doctoral dissertation). Université Paris-Saclay (ComUE).

Courrech du Pont, S., Gondret, P., Perrin, B., & Rabaud, M. (2003). Wall effects on granular heap stability. *Europhysics Letters*, *61*(4), 492–498. https://doi.org/10.1209/epl/i2003-00156-5

Dammeier, F., Moore, J. R., Haslinger, F., & Loew, S. (2011). Characterization of alpine rockslides using statistical analysis of seismic signals. *Journal of Geophysical Research*, *116*(F4), F04024. https://doi.org/10.1029/2011JF002037

de Haas, T., Åberg, A. S., Walter, F., & Zhang, Z. (2021). Deciphering seismic and normal-force fluctuation signatures of debris flows: An experimental assessment of effects of flow composition and dynamics. *Earth Surface Processes and Landforms*, *46*(11), 2195–2210. https://doi.org/10.1002/esp.5168

Delannay, R., Valance, A., Mangeney, A., Roche, O., & Richard, P. (2017). Granular and particle-laden flows: From laboratory experiments to field observations. *Journal of Physics D: Applied Physics*, *50*(5), 053001. https://doi.org/10.1088/1361-6463/50/5/053001

Deparis, J., Jongmans, D., Cotton, F., Baillet, L., Thouvenot, F., & Hantz, D. (2008). Analysis of rock-fall and rock-fall avalanche seismograms in the French Alps. *Bulletin of the Seismological Society of America*, *98*(4), 1781–1796. https://doi.org/10.1785/0120070082

de Richter, S. K., Zaitsev, V. Y., Richard, P., Delannay, R., Le Caër, G., & Tournat, V. (2010). Experimental evidence of ageing and slow restoration of the weak-contact configuration in tilted 3D granular packings. *Journal of Statistical Mechanics: Theory and Experiment*, *2010*(11), P11023. https://doi.org/10.1088/1742-5468/2010/11/P11023

Durand, V., Mangeney, A., Haas, F., Jia, X., Bonilla, F., Peltier, A., et al. (2018). On the link between external forcings and slope instabilities in the piton de la fournaise summit crater, Reunion Island. *Journal of Geophysical Research: Earth Surface*, *123*(10), 2422–2442. https://doi.org/10.1029/2017jf004507

Ekström, G., & Stark, C. P. (2013). Simple scaling of catastrophic landslide dynamics. *Science*, *339*(6126), 1416–1419. https://doi.org/10.1126/science.1232887

Farin, M., Mangeney, A., de Rosny, J., Toussaint, R., Sainte-Marie, J., & Shapiro, N. M. (2016). Experimental validation of theoretical methods to estimate the energy radiated by elastic waves during an impact. *Journal of Sound and Vibration*, *362*, 176–202. https://doi.org/10.1016/j.jsv.2015.10.003

Farin, M., Mangeney, A., de Rosny, J., Toussaint, R., & Trinh, P.-T. (2018). Link between the dynamics of granular flows and the generated seismic signal: Insights from laboratory experiments. *Journal of Geophysical Research: Earth Surface*, *123*(6), 1407–1429. https://doi.org/10.1029/2017JF004296

Farin, M., Mangeney, A., de Rosny, J., Toussaint, R., & Trinh, P.-T. (2019). Relations between the characteristics of granular column collapses and that of the generated high-frequency seismic signal. *Journal of Geophysical Research: Earth Surface*, *124*, 2987–3021. https://doi.org/10.1029/2019JF005258

Farin, M., Mangeney, A., Toussaint, R., de Rosny, J., Shapiro, N. M., Dewez, T., et al. (2015). Characterization of rockfalls from seismic signal: Insights from laboratory experiments. *Journal of Geophysical Research: Solid Earth*, *120*(10), 7102–7137. https://doi.org/10.1002/2015JB012331

Farin, M., Tsai, V. C., Lamb, M. P., & Allstadt, K. E. (2019). A physical model of the high-frequency seismic signal generated by debris flows. *Earth Surface Processes and Landforms*, *44*(13), 2529–2543. https://doi.org/10.1002/esp.4677

Favreau, P., Mangeney, A., Lucas, A., Crosta, G., & Bouchut, F. (2010). Numerical modeling of landquakes. *Geophysical Research Letters*, *37*(15), L15305. https://doi.org/10.1029/2010GL043512

Fernández-Nieto, E. D., Garres-Díaz, J., Mangeney, A., & Narbona-Reina, G. (2018). 2d granular flows with the μ (i) rheology and side walls friction: A well-balanced multilayer discretization. *Journal of Computational Physics*, *356*, 192–219. https://doi.org/10.1016/j.jcp.2017.11.038

Gardel, E., Sitaridou, E., Facto, K., Keene, E., Hattam, K., Easwar, N., & Menon, N. (2009). Dynamical fluctuations in dense granular flows. *Philosophical Transactions of the Royal Society of London: Mathematical, Physical and Engineering Sciences*, *367*(1909), 5109–5121. https://doi.org/10.1098/rsta.2009.0189

GDR MiDi. (2004). On dense granular flows. *The European Physical Journal E*, *14*(4), 341–365. https://doi.org/10.1140/epje/i2003-10153-0

Gimbert, F., Tsai, V., & Lamb, M. (2014). A physical model for seismic noise generation by turbulent flow in rivers. *Journal of Geophysical Research: Earth Surface*, *119*(10), 2209–2238. https://doi.org/10.1007/s10035-017-0738-1

Glasser, B. J., & Goldhirsch, I. (2001). Scale dependence, correlations, and fluctuations of stresses in rapid granular flows. *Physics of Fluids*, *13*(2), 407–420. https://doi.org/10.1063/1.1338543

Goldhirsch, I. (2008). Introduction to granular temperature. *Powder Technology*, *182*(2), 130–136. (Granular Temperature). https://doi.org/10.1016/j.powtec.2007.12.002

Gollin, D., Berzi, D., & Bowman, E. T. (2017). Extended kinetic theory applied to inclined granular flows: Role of boundaries. *Granular Matter*, *19*(3), 56. https://doi.org/10.1007/s10035-017-0738-1

Gollin, D., Bowman, E., & Shepley, P. (2015a). Granular temperature measurements of uniform granular flows. In *Deformation characteristics of geomaterials*. https://doi.org/10.3233/978-1-61499-601-9-647

Gollin, D., Bowman, E., & Shepley, P. (2015b). Methods for the physical measurement of collisional particle flows. In *Iop conference series: Earth and environmental science* (Vol. 26). https://doi.org/10.1088/1755-1315/26/1/012017

Hanes, D., & Walton, O. (2000). Simulations and physical measurements of glass spheres flowing down a bumpy incline. *Powder Technology*, *109*(1), 133–144. https://doi.org/10.1016/S0032-5910(99)00232-6

Hibert, C., Ekström, G., & Stark, C. (2017). The relationship between bulk-mass momentum and short-period seismic radiation in catastrophic landslides. *Journal of Geophysical Research: Earth Surface*, *122*(5), 1201–1215. https://doi.org/10.1002/2016JF004027

Hibert, C., Malet, J.-P., Bourrier, F., Provost, F., Berger, F., Bornemann, P., et al. (2017). Single-block rockfall dynamics inferred from seismic signal analysis. *Earth Surface Dynamics*, *5*(2), 283–292. https://doi.org/10.5194/esurf-5-283-2017

Hibert, C., Mangeney, A., Grandjean, G., Baillard, C., Rivet, D., Shapiro, N. M., et al. (2014). Automated identification, location, and volume estimation of rockfalls at piton de la fournaise volcano. *Journal of Geophysical Research: Earth Surface*, *119*(5), 1082–1105. https://doi.org/10.1002/2013JF002970

Hibert, C., Mangeney, A., Grandjean, G., Peltier, A., DiMuro, A., Shapiro, N. M., et al. (2017). Spatio-temporal evolution of rockfall activity from 2007 to 2011 at the piton de la fournaise volcano inferred from seismic data. *Journal of Volcanology and Geothermal Research*, *333*, 36–52. https://doi.org/10.1016/j.jvolgeores.2017.01.007

Hibert, C., Mangeney, A., Grandjean, G., & Shapiro, N. M. (2011). Slope instabilities in dolomieu crater, réunion island: From seismic signals to rockfall characteristics. *Journal of Geophysical Research*, *116*(F4), F04032. https://doi.org/10.1029/2011JF002038

Hill, K. M., & Tan, D. S. (2014). Segregation in dense sheared flows: Gravity, temperature gradients, and stress partitioning. *Journal of Fluid Mechanics*, *756*, 54–88. https://doi.org/10.1017/jfm.2014.271

Hostler, S. R. (2004). *Wave propagation in granular materials (Unpublished doctoral dissertation)*. California Institute of Technology.

Hostler, S. R., & Brennen, C. E. (2005). Pressure wave propagation in a granular bed. *Physical Review*, *72*(3), 031303. https://doi.org/10.1103/PhysRevE.72.031303

Huang, C.-J., Shieh, C.-L., & Yin, H.-Y. (2004). Laboratory study of the underground sound generated by debris flows. *Journal of Geophysical Research*, *109*(F1), F01008. https://doi.org/10.1029/2003JF000048

Huang, C.-J., Yin, H.-Y., Chen, C.-Y., Yeh, C.-H., & Wang, C.-L. (2007). Ground vibrations produced by rock motions and debris flows. *Journal of Geophysical Research*, *112*(F2), F02014. https://doi.org/10.1029/2005JF000437

Hunt, M. L., & Vriend, N. M. (2010). Booming sand dunes. *Annual Review of Earth and Planetary Sciences*, *38*(1), 281–301. https://doi.org/10.1146/annurev-earth-040809-152336

Jacob, X., Aleshin, V., Tournat, V., Leclaire, P., Lauriks, W., & Gusev, V. E. (2008). Acoustic probing of the jamming transition in an unconsolidated granular medium. *Physical Review Letters*, *100*(15), 158003. https://doi.org/10.1103/PhysRevLett.100.158003

Johnson, K. L. (1987). *Contact mechanics*. Cambridge university press. https://doi.org/10.1017/CBO9781139171731

Jop, P., Forterre, Y., & Pouliquen, O. (2005). Crucial role of sidewalls in granular surface flows: Consequences for the rheology. *Journal of Fluid Mechanics*, *541*(-1), 167–192. https://doi.org/10.1017/S0022112005005987

Jop, P., Forterre, Y., & Pouliquen, O. (2007). Initiation of granular surface flows in a narrow channel. *Physics of Fluids*, *19*(8), 088102. https://doi.org/10.1063/1.2753111

Josserand, C., Lagrée, P.-Y., & Lhuillier, D. (2004). Stationary shear flows of dense granular materials: A tentative continuum modelling. *The European Physical Journal E*, *14*(2), 127–135. https://doi.org/10.1140/epje/i2003-10141-4

Kanamori, H., & Given, J. W. (1982). Analysis of long-period seismic waves excited by the May 18, 1980, eruption of Mount St. Helens—A terrestrial monopole? *Journal of Geophysical Research*, *87*(B7), 5422–5432. https://doi.org/10.1029/jb087ib07p05422

Kean, J. W., Coe, J. A., Coviello, V., Smith, J. B., McCoy, S. W., & Arattano, M. (2015). Estimating rates of debris flow entrainment from ground vibrations. *Geophysical Research Letters*, *42*(15), 6365–6372. https://doi.org/10.1002/2015GL064811

Kharel, P., & Rognon, P. (2017). Vortices enhance diffusion in dense granular flows. *Physical Review Letters*, *119*(17), 178001. https://doi.org/10.1103/PhysRevLett.119.178001

Kolmogorov, A. N. (1941). The local structure of turbulence in incompressible viscous fluid for very large Reynolds numbers. *Doklady Akademii Nauk SSSR*, *30*, 301–305.

Kuehnert, J., Mangeney, A., Capdeville, Y., Métaxian, J. P., Bonilla, L. F., Stutzmann, E., et al. (2020). Simulation of topography effects on rockfall-generated seismic signals: Application to piton de la fournaise volcano. *Journal of Geophysical Research: Solid Earth*, *125*(10), e2020JB019874. https://doi.org/10.1029/2020JB019874

Kuehnert, J., Mangeney, A., Capdeville, Y., Vilotte, J. P., Stutzmann, E., Chaljub, E., et al. (2021). Locating rockfalls using inter-station ratios of seismic energy at dolomieu crater, piton de la fournaise volcano. *Journal of Geophysical Research: Earth Surface*, *126*(4), e2020JF005715. https://doi.org/10.1029/2020JF005715

Lai, V. H., Tsai, V. C., Lamb, M. P., Ulizio, T. P., & Beer, A. R. (2018). The seismic signature of debris flows: Flow mechanics and early warning at Montecito, California. *Geophysical Research Letters*, *45*(11), 5528–5535. https://doi.org/10.1029/2018GL077683

La Rocca, M., Galluzzo, D., Saccorotti, G., Tinti, S., Cimini, G. B., & Del Pezzo, E. (2004). Seismic signals associated with landslides and with a tsunami at Stromboli volcano, Italy. *Bulletin of the Seismological Society of America*, *94*(5), 1850–1867. https://doi.org/10.1785/012003238

Leclercq, M., Picart, P., Penelet, G., & Tournat, V. (2017). Investigation of 3d surface acoustic waves in granular media with 3-color digital holography. *Journal of Applied Physics*, *121*(4), 045112. https://doi.org/10.1063/1.4974950

Legland, J.-B., Tournat, V., Dazel, O., Novak, A., & Gusev, V. (2012). Linear and nonlinear biot waves in a noncohesive granular medium slab: Transfer function, self-action, second harmonic generation. *Journal of the Acoustical Society of America*, *113*(6), 4292–4303. https://doi.org/10.1121/1.4712020

Levy, C., Mangeney, A., Bonilla, F., Hibert, C., Calder, E. S., & Smith, P. J. (2015). Friction weakening in granular flows deduced from seismic records at the Soufrière hills volcano, Montserrat. *Journal of Geophysical Research: Solid Earth*, *120*(11), 7536–7557. https://doi.org/10.1002/2015JB012151

Lherminier, S., Planet, R., Simon, G., Vanel, L., & Ramos, O. (2014). Revealing the structure of a granular medium through ballistic sound propagation. *Physical Review Letters*, *113*(9), 098001. https://doi.org/10.1103/physrevlett.113.098001

Lin, Y.-N., Sieh, K., & Stock, J. (2010). Submarine landslides along the malacca strait-mergui basin shelf margin: Insights from sequence-stratigraphic analysis. *Journal of Geophysical Research*, *115*(12), B12102. https://doi.org/10.1029/2009JB007050

Liu, C.-h., & Nagel, S. R. (1993). Sound in a granular material: Disorder and nonlinearity. *Physical Review B*, *48*(21), 15646–15650. https://doi.org/10.1103/physrevb.48.15646

Lucas, A., Mangeney, A., & Ampuero, J.-P. (2014). Frictional velocity-weakening in landslides on Earth and on other planetary bodies. *Nature Communications*, *5*(1), 3417. https://doi.org/10.1038/ncomms4417

Mandal, S., & Khakhar, D. V. (2017). A sidewall friction driven ordering transition in granular channel flows: Implications for granular rheology. arXiv preprint arXiv:1706.05503.

Martin, R., Bodet, L., Tournat, V., & Rejiba, F. (2018). Seismic wave propagation in nonlinear viscoelastic media using the auxiliary differential equation method. *Geophysical Journal International*, *216*(1), 453–469. https://doi.org/10.1093/gji/ggy441

Michlmayr, G., Cohen, D., & Or, D. (2013). Shear-induced force fluctuations and acoustic emissions in granular material. *Journal of Geophysical Research: Solid Earth*, *118*(12), 6086–6098. https://doi.org/10.1002/2012JB009987

Moretti, L., Allstadt, K., Mangeney, A., Capdeville, Y., Stutzmann, E., & Bouchut, F. (2015). Numerical modeling of the mount meager landslide constrained by its force history derived from seismic data. *Journal of Geophysical Research: Solid Earth*, *120*(4), 2579–2599. https://doi.org/10.1002/2014JB011426

Moretti, L., Mangeney, A., Capdeville, Y., Stutzmann, E., Huggel, C., Schneider, D., & Bouchut, F. (2012). Numerical modeling of the mount Steller landslide flow history and of the generated long period seismic waves. *Geophysical Research Letters*, *39*(16), L16402. https://doi.org/10.1029/2012GL052511

Moretti, L., Mangeney, A., Walter, F., Capdeville, Y., Bodin, T., Stutzmann, E., et al. (2020). Numerical modeling of the mount Steller landslide flow history and of the generated long period seismic waves. *Geophysical Research Letters*, *39*(16), L16402. https://doi.org/10.1029/2012GL052511

Mouraille, O., & Luding, S. (2008). Sound wave propagation in weakly polydisperse granular materials. *Ultrasonics*, *48*(6), 498–505. https://doi.org/10.1016/j.ultras.2008.03.009

Norris, R. D. (1994). Seismicity of rockfalls and avalanches at three Cascade Range volcanoes: Implications for seismic detection of hazardous mass movements. *Bulletin of the Seismological Society of America*, *84*(6), 1925.

Okal, E. A. (1990). Single forces and double-couples: A theoretical review of their relative efficiency for the excitation of seismic and tsunami waves. *Journal of Physics of the Earth*, *38*(6), 445–474. https://doi.org/10.4294/jpe1952.38.445

Okuda, S., Suwa, H., Okunishi, K., Yokoyama, K., & Nakano, M. (1980). Observations on the motion of a debris flow and its geomorphological effect. *Zeitschrift für Geomorphologie, Supplement*, *35*, 142–163.

Orpe, A. V., & Kudrolli, A. (2007). Velocity correlations in dense granular flows observed with internal imaging. *Physical Review Letters*, *98*(23), 238001. https://doi.org/10.1103/PhysRevLett.98.238001

Pouliquen, O. (2004). Velocity correlations in dense granular flows. *Physical Review Letters*, *93*(24), 248001. https://doi.org/10.1103/PhysRevLett.93.248001

Royer, D., & Dieulesaint, E. (2000). *Elastic waves in solids i: Free and guided propagation*. Springer Berlin Heidelberg.

Sarno, L., Papa, M. N., Villani, P., & Tai, Y.-C. (2016). An optical method for measuring the near-wall volume fraction in granular dispersions. *Granular Matter*, *18*(4), 80. https://doi.org/10.1007/s10035-016-0676-3

Schneider, D., Bartelt, P., Caplan-Auerbach, J., Christen, M., Huggel, C., & McArdell, B. W. (2010). Insights into rock-ice avalanche dynamics by combined analysis of seismic recordings and a numerical avalanche model. *Journal of Geophysical Research*, *115*(F4), F04026. https://doi.org/10.1029/2010JF001734

Staron, L. (2008). Correlated motion in the bulk of dense granular flows. *Physical Review*, *77*(5), 051304. https://doi.org/10.1103/PhysRevE.77.051304

Taberlet, N., Richard, P., Valance, A., Losert, W., Pasini, J. M., Jenkins, J. T., & Delannay, R. (2003). Superstable granular heap in a thin channel. *Physical Review Letters*, *91*(26), 264301. https://doi.org/10.1103/PhysRevLett.91.264301

Taylor, S., & Brodsky, E. E. (2017). Granular temperature measured experimentally in a shear flow by acoustic energy. *Physical Review*, *96*(3), 032913. https://doi.org/10.1103/PhysRevE.96.032913

Thielicke, W., & Stamhuis, E. (2014). Pivlab–towards user-friendly, affordable and accurate digital particle image velocimetry in MATLAB. *Journal of Open Research Software*, *2*(1). https://doi.org/10.5334/jors.bl

van den Wildenberg, S., van Hecke, M., & Jia, X. (2013). Evolution of granular packings by nonlinear acoustic waves. *EPL*, *101*(1), 14004. https://doi.org/10.1209/0295-5075/101/14004

Voronina, V., & Horoshenkov, K. (2004). Acoustic properties of unconsolidated granular mixes. *Applied Acoustics*, *65*(7), 673–691. https://doi.org/10.1016/j.apacoust.2003.12.002

Weinhart, T., Hartkamp, R., Thornton, A. R., & Luding, S. (2013). Coarse-grained local and objective continuum description of three-dimensional granular flows down an inclined surface. *Physics of Fluids*, *25*(7), 070605. https://doi.org/10.1063/1.4812809

Westerweel, J., & Scarano, F. (2005). Universal outlier detection for PIV data. *Experiments in Fluids*, *39*(6), 1096–1100. https://doi.org/10.1007/s00348-005-0016-6

Yamada, M., Kumagai, H., Matsushi, Y., & Matsuzawa, T. (2013). Dynamic landslide processes revealed by broadband seismic records. *Geophysical Research Letters*, *40*(12), 2998–3002. https://doi.org/10.1002/grl.50437

Yamada, M., Mangeney, A., Matsushi, Y., & Matsuzawa, T. (2018). Estimation of dynamic friction and movement history of large landslides. *Landslides*, *15*(10), 1963–1974. https://doi.org/10.1007/s10346-018-1002-4

Yamada, M., Mangeney, A., Matsushi, Y., & Moretti, L. (2016). Estimation of dynamic friction of the akatani landslide from seismic waveform inversion and numerical simulation. *Geophysical Journal International*, *206*(3), 1479–1486. https://doi.org/10.1093/gji/ggw216

Zaitsev, V. Y., Gusev, V. E., Tournat, V., & Richard, P. (2008). Slow relaxation and aging phenomena at the nanoscale in granular materials. *Physical Review Letters*, *112*(10), 108302. https://doi.org/10.1103/PhysRevLett.112.108302

Zaitsev, V. Y., Gusev, V. E., Tournat, V., & Richard, P. (2014). Slow Relaxation and Aging Phenomena at the Nanoscale in Granular Materials. *Physical Review Letters*, *112*, 108302. https://doi.org/10.1103/PhysRevLett.112.108302

Zaitsev, V. Y., Richard, P., Delannay, R., Tournat, V., & Gusev, V. E. (2008). Pre-avalanche structural rearrangements in the bulk of granular medium: Experimental evidence. *Europhysics Letters*, *83*(6), 64003. https://doi.org/10.1209/0295-5075/83/64003

Zhang, Z., Walter, F., McArdell, B. W., de Haas, T., Wenner, M., Chmiel, M., & He, S. (2021). Analyzing bulk flow characteristics of debris flows using their high frequency seismic signature. *Journal of Geophysical Research: Solid Earth*, *126*(12), e2021JB022755. https://doi.org/10.1029/2021JB022755

Zhao, J., Moretti, L., Mangeney, A., Stutzmann, E., Kanamori, H., Capdeville, Y., et al. (2015). Model space exploration for determining landslide source history from long-period seismic data. *Pure and Applied Geophysics*, *172*(2), 389–413. https://doi.org/10.1007/s00024-014-0852-5